Minkowski Tensors in Redshift Space—Beyond the Plane-parallel Approximation

Stephen Appleby[1,2], Joby P. Kochappan[1] , Pravabati Chingangbam[3,4], and Changbom Park[4]
[1] Asia Pacific Center for Theoretical Physics, Pohang, 37673, Republic of Korea; stephen.appleby@apctp.org, joby.kochappan@apctp.org
[2] Department of Physics, POSTECH, Pohang 37673, Republic of Korea
[3] Indian Institute of Astrophysics, Koramangala II Block, Bangalore 560 034, India
[4] School of Physics, Korea Institute for Advanced Study, 85 Hoegiro, Dongdaemun-gu, Seoul, 02455, Republic of Korea

Abstract

The Minkowski tensors (MTs) can be used to probe anisotropic signals in a field, and are well suited for measuring the redshift-space distortion (RSD) signal in large-scale structure catalogs. We consider how the linear RSD signal can be extracted from a field without resorting to the plane-parallel approximation. A spherically redshift-space distorted field is both anisotropic and inhomogeneous. We derive expressions for the two-point correlation functions that elucidate the inhomogeneity, and then explain how the breakdown of homogeneity impacts the volume and ensemble averages of the tensor Minkowski functionals. We construct the ensemble average of these quantities in curvilinear coordinates and show that the ensemble and volume averages can be approximately equated, but this depends on our choice of definition of the volume average of a tensor and the radial distance between the observer and field. We then extract the tensor Minkowski functionals from spherically redshift-space distorted, Gaussian random fields and gravitationally evolved dark matter density fields at $z = 0$ to test if we can successfully measure the Kaiser RSD signal. For the dark matter field, we find a significant, $\sim 10\%$ anomalous signal in the MT component parallel to the line of sight that is present even on large scales $R_{\rm G} \gtrsim 15$ Mpc, in addition to the Kaiser effect. This is due to the line-of-sight component of the MT being significantly contaminated by the Finger of God effect, which can be approximately modeled by an additional damping term in the cumulants.

Unified Astronomy Thesaurus concepts: Cosmology (343)

1. Introduction

The tensor Minkowski functionals are a rank-p generalization of the scalar Minkowski functionals (Santalo 1976; McMullen 1997; Alesker 1999; Beisbart et al. 2001a, 2002; Hug et al. 2008; Schroder-Turk et al. 2013, 2010). Being tensors, they are sensitive to directionally dependent signals in data and have found application in a number of disciplines such as material science (Becker et al. 2003; Olszowka et al. 2006; Rehse et al. 2008). The scalar Minkowski functionals and associated morphological statistics have a long and storied history within cosmology (Melott et al. 1989; Gott et al. 1990; Park & Gott 1991; Mecke et al. 1994; Schmalzing & Buchert 1997; Sahni et al. 1998; Schmalzing & Gorski 1998; Park et al. 1992, 2001; Bharadwaj et al. 2000; Park & Kim 2010; van de Weygaert et al. 2011a; Zunckel et al. 2011; Park et al. 2013; van de Weygaert et al. 2011b; Shivshankar et al. 2015; Pranav et al. 2017, 2019a, 2019b; Feldbrugge et al. 2019; Munshi et al. 2021; Wilding et al. 2021), but the tensors are less widely adopted. They were initially introduced in Beisbart et al. (2001b, 2001a, 2002) to provide a measure of substructure of galaxy clusters and spiral galaxies. In the mathematics literature, they are defined for structures on flat Euclidean space. In two dimensions, the definition of the translation invariant rank (2) Minkowski tensors (MTs) were generalized to structures on the two-sphere in Chingangbam & Yogendran (2017). More recently, they have been applied to cosmological scale fields (Chingangbam & Yogendran 2017; Ganesan & Chingangbam 2017; Appleby et al. 2018a, 2018b;

Rahman et al. 2021), cosmic microwave background (CMB) temperature and polarization data (Ganesan & Chingangbam 2017; Joby et al. 2019; Kochappan et al. 2021; Goyal et al. 2020; Goyal & Chingangbam 2021), and the fields of the epoch of reionization (Kapahtia et al. 2018, 2019, 2021). In addition, the authors have written a series of papers on the application of the MTs to the low redshift matter density field as traced by galaxies (Appleby et al. 2018a, 2018b). The ensemble average of the MTs measured from isotropic and anisotropic, Gaussian random fields were considered in Chingangbam & Yogendran (2017), Appleby et al. (2018b), and Chingangbam et al. (2021). Anisotropic random fields were subsequently explored further in Klatt et al. (2022), including higher-rank statistics. Numerical algorithms with which to extract the MTs from two-dimensional fields can be found in Schroder-Turk et al. (2010), Appleby et al. (2018a), and Schaller et al. (2020).

In real space, galaxies are assumed to be distributed in a statistically isotropic and homogeneous manner. The cosmic web is locally anisotropic, with filaments feeding matter into nodes, and extended structures aligning on two-dimensional walls. In this picture, isotropy of the matter distribution means that there is no globally preferred direction within the filamentary large-scale structure, when averaging over a volume that is large compared to the typical scale of the structures. This statistical isotropy is an axiom within cosmology, motivated by observations of the CMB. For any large-scale structure distribution, we can always find a frame of reference in which the observer is at rest with respect to the data using a velocity correction. Conventionally observed redshifts are adjusted to place large-scale structure catalogs in the rest frame of the CMB temperature fluctuations, but recent results suggest that high redshift radio sources require a different velocity correction (Secrest et al. 2021, 2022). If

robust, this apparent breakdown in the cosmological principle highlights the importance of testing standard model assumptions such as isotropy and homogeneity (Aluri et al. 2022).

Even if the large-scale distribution of the matter field in real space is isotropic, the observed distribution of galaxies is contaminated by their peculiar velocity along the line of sight. This phenomenon was first described in early pioneering works (Kaiser 1987), and is referred to as the redshift-space distortion (RSD) effect. The RSD effect perturbs the apparent position of galaxies in redshift space only along the line of sight, and hence has rotational symmetry around the central observer. However, it leads to a global alignment of structures in the excursion sets of the density field along the line of sight. This alignment of structures in the field is what we refer to as anisotropy in the context of MTs. A significant body of literature has subsequently been devoted to understanding the effect of RSD on the two-point statistics (Hamilton 1997; Scoccimarro 2004; Weinberg et al. 2013) and other quantities (Matsubara 1996; Codis et al. 2013).

There are two phenomena commonly associated with RSD. On small scales $\lesssim \mathcal{O}(1 \text{ Mpc})$, the Finger of God effect describes the scatter of galaxy positions within bound structures due to their stochastic velocity components (Jackson 1972). In addition, coherent in-fall into overdensities—and corresponding outflow from underdensities—occurs on all scales. The latter phenomenon, dubbed the Kaiser effect (Kaiser 1987), can be described using the linear perturbation theory on large scales. The density field in the late universe is non-Gaussian due to the nonlinear nature of gravitational collapse, but by smoothing the field on sufficiently large scales, one can treat the field as approximately Gaussian and the RSD effect as approximately Kaiserian. The anisotropic effect of RSD contains information regarding the growth rate of structure, due to the fact that the signal is a measure of the in-fall rate of matter into gravitational potentials. When modeling the large-scale-smoothed density field, the complicated physics associated with bound and merging structures is reduced to a simple phenomenological parameterization of the Finger of God effect (Jackson 1972).

This work is a continuation of a series of papers by the authors, in which we consider the impact of RSD on the tensor Minkowski functionals. In Appleby et al. (2018b), the authors described a numerical algorithm used to extract the Minkowski functionals and Cartesian tensors from any three-dimensional field. In Appleby et al. (2019), we constructed the ensemble expectation value of the MTs in redshift space, in the linearized, plane-parallel Kaiser limit and for Gaussian random fields. The latter paper used the so-called *distant observer* approximation, making the simplifying assumption that the field is sufficiently remote from the observer and localized in the direction, so that each point in the field practically shares a common line-of-sight vector along which the RSD operator acts. This, in conjunction with periodic boundary conditions, renders the field anisotropic but homogeneous, and the sky flat for computational purposes. In reality, the radial nature of the RSD signal generates an inhomogeneous field.

The purpose of this work is two-fold. First, we generalize the calculation in Appleby et al. (2019) to account for the radial nature of the RSD signal. We calculate the ensemble average of the MTs in spherical coordinates, for a field that has been subjected to a radial RSD correction. The calculation requires a careful reappraisal of the Cartesian tensor analysis of

Appleby et al. (2019) to account for the vagaries of curvilinear coordinate systems. In addition, a radial signal is inherently inhomogeneous, and this will have consequences for the assumption of ergodicity that is frequently applied to cosmological fields. Second, we use gravitationally evolved, dark matter N-body simulations to construct mildly non-Gaussian density fields by smoothing over large scales $15 \text{ Mpc} < R_G < 45 \text{ Mpc}$. We compare the extracted MT statistics to their Gaussian expectation values, to determine the scale at which the analytic prediction can be used. This analysis serves as a precursor to a forthcoming paper, in which we will extract these statistics from the BOSS galaxy data and infer the growth rate from the RSD signal.

The paper will proceed as follows. We review the definition of the rank (2) MTs in Section 2, and also provide details on our approach to ensemble averaging. In Section 3, we restate the main results of Appleby et al. (2019); the ensemble average of the MTs in globally plane-parallel redshift space. In Section 4, we expand the analysis and derive the expectation value of the MTs in a spherical coordinate system for a field with radial anisotropy relative to a central observer. We repeat this analysis in a Cartesian coordinate system in Section 5. In Section 6, we extract the MTs from dark matter particle snapshot boxes after applying a radial RSD correction, to test the scale at which the Gaussian limit is approached and the magnitude of the non-Gaussian corrections. We also compare plane-parallel and radial anisotropic signals. We discuss our results in Section 7.

Throughout this work, in the main body of the text, we focus on the particular MT $W_1^{0,2}$, because it is computationally simpler, and we expect that it will provide superior constraining power (Appleby et al. 2019). A second linearly independent, translation invariant MT in three dimensions $W_2^{0,2}$ has some additional complications because it is a function of the second derivative of the field. For completeness we include a brief analysis of $W_2^{0,2}$ in Appendix A. The rotation of the spherical basis vectors relative to a great arc tangent vector is presented in Appendix B, and finally some useful identities regarding spherical harmonics and Bessel functions are provided in Appendix C.

2. Translation Invariant Minkowski Tensors in Three Dimensions

The MTs have been elucidated in numerous papers, and we direct the reader to Schroder-Turk et al. (2013) for details on the quantities used in this work. Briefly, in three dimensions, we define an excursion set Q for a field $\delta(x)$ on a manifold $\mathbb{M}$ as

$$Q = \{x \in \mathbb{M}: \delta(x) \geqslant \delta_t\}, \tag{1}$$

where δ_t is a chosen density threshold value. Initially we take the manifold $\mathbb{M}$ to be three-dimensional Euclidean space $\mathbb{R}^3$. We then define two translation invariant, rank (2) tensors as

$$W_1^{0,2} \equiv \frac{1}{6V} \int_{\partial Q} \hat{\boldsymbol{n}}^2 dA; \tag{2}$$

$$W_2^{0,2} \equiv \frac{1}{3\pi V} \int_{\partial Q} G_2 \hat{\boldsymbol{n}}^2 dA, \tag{3}$$

where the boundary ∂Q of Q is a two-dimensional isofield surface defined by $\delta(x) = \delta_t$. The vector $\hat{\boldsymbol{n}}$ is the unit normal vector, and G_2 is the mean curvature at each point of the surface ∂Q. We define the symmetric tensor product as

$\hat{\boldsymbol{n}}^2 = \hat{\boldsymbol{n}} \otimes \hat{\boldsymbol{n}} = (\hat{n}_i \hat{n}_j + \hat{n}_j \hat{n}_i)/2$. The vector $\hat{\boldsymbol{n}}$ is an element of the cotangent space at each point on $\mathbb{R}^3$. Since addition is defined only for vectors or tensors that belong to the same vector space, in order to perform these integrals, we must transport all normal vectors to a fiducial point, and addition is then carried out in the cotangent space at that point. This is a trivial step when the manifold is flat space. $W_1^{0,2}$ and $W_2^{0,2}$ are invariant under translation of the coordinates, which ensures that they are independent of the choice of fiducial point on $\mathbb{R}^3$. If the manifold is curved, then the integrals defined in the expressions from Equations (2), (3) require a fiducial point at which the average is taken to be specified, as well as the choice of transport path. These details will be important later and considered in Section 4.2.

We will measure $W_1^{0,2}$ and $W_2^{0,2}$ from dark matter point distributions, which are smoothed with a Gaussian kernel to generate a continuous matter field with background density ρ_m and fluctuations $\delta(x)$. The fluctuations satisfy $\langle \delta \rangle = 0$, where $\langle ... \rangle$ represents the ensemble average of this random field. When smoothed on large scales,[5] $\delta(x)$ is assumed to be well approximated as a Gaussian random field, but on small scales, non-Gaussianities are present due to the mode coupling arising from the nonlinear nature of gravitational collapse. In this work, we are chiefly concerned with the large-scale limit of the density field, where Gaussian statistics can be applied. The non-Gaussian corrections require further study and are beyond the scope of this work. For the remainder of the paper, we will focus specifically on the MT $W_1^{0,2}$, and consign the more complicated $W_2^{0,2}$ statistic to Appendix A.

An alternative approach to the one considered in this work is to generate a triangulated mesh directly from the point distribution and extract the MTs from this manifold (Klatt et al. 2016). This approach preserves all information in the distribution, but also includes the noise component due to finite sampling. However, since the shot noise contribution is expected to be isotropic, working with the point distribution directly may be optimal to extract anisotropic signals. If we wish to relate the measured volume average with large-scale cosmological perturbation theory, smoothing is required. A related issue was studied within the context of the CMB E-mode data (Kochappan et al. 2021).

Following Schmalzing & Buchert (1997), Schmalzing & Gorski (1998), we perform a surface-to-volume integral transform and use $\hat{n}_i = \delta_i / |\nabla \delta|$ to rewrite Equation (2), as

$$W_1^{0,2}|_i{}^j = \frac{1}{6V} \int_V dV \, \delta_D(\delta - \delta_t) \frac{\delta_i \delta^j}{|\nabla \delta|}, \qquad (4)$$

where we use shorthand notation for the gradients of the field $\delta_i = \nabla_i \delta$, and δ_D is the Dirac delta function. Given that δ is assumed to be a smooth random field, its derivatives and in particular the vector $\delta_i / |\nabla \delta|$ are well defined at all points over the volume V. The right-hand side of Equation (4) is the volume average of the rank (1, 1) tensor

$$w_i{}^j = \frac{1}{6} \frac{\delta_i \delta^j}{|\nabla \delta|} \delta_D(\delta - \delta_t), \qquad (5)$$

---

where the delta function $\delta_D(\delta - \delta_t)$ can be defined in a distributional sense when constructing the ensemble average or approximately discretized when taking the volume average (Schmalzing & Buchert 1997). We denote the volume average of this tensor as $\bar{w}_i{}^j \equiv W_1^{0,2}|_i{}^j$.

2.1. Ensemble Average and Ergodicity

First, we review the steps made in calculating the ensemble average of w_i^j, because there are some subtleties that will become important later. The purpose of this subsection is to highlight the assumptions that are made when deriving the ensemble average of w_i^j, and then equating this quantity to the volume average that we measure from cosmological data.

The ensemble average $\langle ... \rangle$ is the linear sum over possible states of the quantity within the brackets, weighted by the probability of that state;

$$\langle w_i{}^j \rangle = \frac{1}{6} \int \Phi(X, \Sigma) \, \delta_D(\delta - \delta_t) \frac{\delta_i \delta^j}{|\nabla \delta|} dX, \qquad (6)$$

where $X = (\delta, \delta_i)$ is shorthand for an array of the field and components of its first derivatives, and $\Phi(X, \Sigma)$ is the underlying probability distribution function (PDF) for X. Here w_i^j is defined at a point on the manifold, so $\Phi(X, \Sigma)$ is the PDF describing the field and its derivatives at a single location. For a Gaussian random field, we have $\Phi(X, \Sigma) \propto \exp[-X^T \Sigma^{-1} X / 2]$, where Σ denotes the covariance between the component fields of X. When integrating over X, all physical information is contained within the inverse covariance matrix Σ^{-1} in $\Phi(X, \Sigma)$. To estimate the ensemble average of w_i^j, we require the covariance matrix Σ.

In cosmological applications, we measure $\bar{w}_i{}^j$ from a data set and then equate this quantity to the theoretically predicted $\langle w_i^j \rangle$. That is, we invoke ergodicity to impose $\langle w_i{}^j \rangle \simeq \bar{w}_i{}^j$. Ergodicity is known to be exact if a field is homogeneous, Gaussian, the two-point correlation ζ of δ satisfies $\zeta(r)|_{r \to \infty} = 0$, and we take the limit $V \to \infty$ (Adler 1981 p145). In reality, cosmological fields occupy a finite volume and have finite resolution, and ergodicity is never exactly realized. We tacitly interpret the volume average of a quantity over a finite domain as providing an unbiased estimate of the ensemble average, with an associated uncertainty related to the finite sampling of the probability distribution.

If the covariance Σ between the fields δ, δ_i contains explicit coordinate dependence, then the ensemble average $\langle w_i^j \rangle$ is sensitive to the position $\boldsymbol{x}$ on the manifold at which we take this average: $\Phi = \Phi(X, \Sigma(\boldsymbol{x}))$. In this case, it is clear that the ensemble average at any given point cannot be equated to the volume average of the same tensor over the entire manifold. The constancy of Σ is a consequence of the fields being homogeneous (see, e.g., Adler 1981; Chingangbam et al. 2021), so when the fields are inhomogeneous, we cannot invoke ergodicity, and generically $\langle w_i{}^j \rangle \neq \bar{w}_i{}^j$. In such a situation, the question of whether we can invoke ergodicity—even approximately—depends on the physical properties of the field, manifold, and coordinate system adopted. In what follows, we will present an example for which $\bar{w}_i{}^j \simeq \langle w_i{}^j \rangle$ is an excellent approximation despite the field being inhomogeneous, and a second example for which $\bar{w}_i{}^j$ completely fails to encapsulate the properties of the ensemble average.

For a homogeneous field, Σ and hence $\langle w_i^j \rangle$ are constant over the entire manifold, and the ergodicity is more naturally

realized. Ambiguity remains in the definition of the volume average of a tensor, which is discussed further in Section 4.2.

3. Review: Plane-parallel Redshift-space Distortions

In Section 4, we will calculate the ensemble average of w_t^j for a Gaussian field that has been subjected to a spherically symmetric RSD operator, but before doing so, we briefly review the plane-parallel result derived in Appleby et al. (2019), aided by earlier work on the Minkowski functionals (Doroshkevich 1970; Adler 1981; Gott et al. 1986; Hamilton et al. 1986; Tomita 1986; Gott et al. 1987; Weinberg et al. 1987; Ryden et al. 1989; Matsubara 1994a, 1994b; Matsubara & Suto 1996; Matsubara 2000; Hikage et al. 2008; Gay et al. 2012).[6]

We take an isotropic and homogeneous Gaussian random field in a periodic box, adopt a Cartesian coordinate system x, y, z with basis vectors $\boldsymbol{e}_x$, $\boldsymbol{e}_y$, $\boldsymbol{e}_z$, and then apply the plane-parallel RSD operator aligned with one of the coordinate axes taken arbitrarily to be $\boldsymbol{e}_z$. We preserve periodicity in $\boldsymbol{e}_z$, so that the field is homogeneous but anisotropic. We simply restate the main results of Appleby et al. (2019), and direct the reader to that work for details of the calculation and Matsubara (1996), Codis et al. (2013) for a detailed analysis of the RSD effect on the scalar functionals.

To linear order in the density fluctuation, the relation between the true position of a tracer particle $\boldsymbol{x}$ and its redshift-space position $\boldsymbol{s}$ is given by

$$\boldsymbol{s} = \boldsymbol{x} + f\boldsymbol{e}_z\,(\boldsymbol{u}.\boldsymbol{e}_z), \qquad (7)$$

where $f = d\ln D/d\ln a$, and D is the linear growth factor, $\boldsymbol{u} = \boldsymbol{v}/(aHf)$, $\boldsymbol{v}$ is the peculiar velocity, and H is the Hubble parameter. We have assumed that every tracer particle is subject to a single, parallel line of sight. In this work, we assume that f is independent of redshift, neglecting its time dependence. In practice, we measure $f\sigma_8$ from galaxy catalogs, which only has mild redshift dependence.

The density field in redshift space $\tilde{\delta}$ can be related to its real space counterpart δ according to

$$\tilde{\delta}(\boldsymbol{k}) = (1 + f\mu^2)\delta(\boldsymbol{k}), \qquad (8)$$

where $\mu = \boldsymbol{k}.\boldsymbol{e}_z/|\boldsymbol{k}|$ is the cosine of the angle between the line of sight and wavenumber $\boldsymbol{k}$. The cumulants of the field $\tilde{\delta}$ and its gradient are given by Matsubara (1996):

$$\langle\tilde{\delta}(\boldsymbol{x}')\tilde{\delta}(\boldsymbol{x})\rangle|_{\boldsymbol{x}'\to\boldsymbol{x}} = \sigma_0^2\left[1 + \frac{2}{3}f + \frac{1}{5}f^2\right]; \qquad (9)$$

$$\langle\tilde{\delta}_x(\boldsymbol{x}')\tilde{\delta}_x(\boldsymbol{x})\rangle|_{\boldsymbol{x}'\to\boldsymbol{x}}$$
$$= \langle\tilde{\delta}_y(\boldsymbol{x}')\tilde{\delta}_y(\boldsymbol{x})\rangle|_{\boldsymbol{x}'\to\boldsymbol{x}} = \sigma_1^2\left[\frac{1}{3} + \frac{2}{15}f + \frac{1}{35}f^2\right]; \quad (10)$$

$$\langle\tilde{\delta}_z(\boldsymbol{x}')\tilde{\delta}_z(\boldsymbol{x})\rangle|_{\boldsymbol{x}'\to\boldsymbol{x}} = \sigma_1^2\left[\frac{1}{3} + \frac{2}{5}f + \frac{1}{7}f^2\right]; \qquad (11)$$

$$\langle\tilde{\delta}(\boldsymbol{x}')\tilde{\delta}_i(\boldsymbol{x})\rangle|_{\boldsymbol{x}'\to\boldsymbol{x}} = 0, \qquad (12)$$

where we have defined the ith isotropic cumulant as

$$\sigma_i^2 = \frac{1}{2\pi^2}\int k^{2i+2}P(k, R_G)dk, \qquad (13)$$

---

[6] See Buchert et al. (2017) for a model-independent approach applying Minkowski functionals to the CMB and using general Hermite expansions of the discrepancy functions with respect to the analytical Gaussian predictions.

and have introduced a Gaussian-smoothed power spectrum $P(k, R_G) = W^2(kR_G)P(k)$, with $W(kR_G) \propto e^{-k^2R_G^2/2}$ for some comoving smoothing scale R_G. The ensemble expectation value of the components of the MT $W_1^{0,2}$ in this particular Cartesian coordinate system, assuming the field is Gaussian, is then Appleby et al. (2019):

$$\langle W_1^{0,2}|_{xx}\rangle$$
$$= \frac{A_0}{4}\left[\frac{(2\lambda^2 - 1)\cosh^{-1}(2\lambda^2 - 1)}{(\lambda^2 - 1)^{3/2}} - \frac{2\lambda}{\lambda^2 - 1}\right]e^{-\nu^2/2}, \quad (14)$$

$$\langle W_1^{0,2}|_{yy}\rangle = \langle W_1^{0,2}|_{xx}\rangle, \qquad (15)$$

$$\langle W_1^{0,2}|_{zz}\rangle = A_0\left(\frac{\lambda^2}{\lambda^2 - 1}\right)\left(\lambda - \frac{\cosh^{-1}\lambda}{\sqrt{\lambda^2 - 1}}\right)e^{-\nu^2/2}, \qquad (16)$$

$$\langle W_1^{0,2}|_{xy}\rangle = \langle W_1^{0,2}|_{xz}\rangle = \langle W_1^{0,2}|_{yz}\rangle = 0, \qquad (17)$$

the constant A_0 is given by

$$A_0 = \frac{\sigma_1}{6\sqrt{3}\,\pi\sigma_0}\sqrt{\frac{105 + 42f + 9f^2}{105 + 70f + 21f^2}}, \qquad (18)$$

and

$$\lambda^2 = \frac{35 + 42f + 15f^2}{35 + 14f + 3f^2}, \qquad (19)$$

and we have introduced the normalized threshold $\nu = \delta_t/\tilde{\sigma}_0$, where $\tilde{\sigma}_0^2 = \langle\tilde{\delta}(\boldsymbol{x}')\tilde{\delta}(\boldsymbol{x})\rangle|_{\boldsymbol{x}'\to\boldsymbol{x}}$. The MT is diagonal in this coordinate system, with discrepant values in the directions perpendicular and parallel to the *line of sight z*. A coordinate transform will generate off-diagonal terms, but the eigenvalues remain invariant. Modulo a noise component due to finite sampling, the eigenvalues are equal to the diagonal elements of the MT in this coordinate system. The properties of the field dictate the form of the MT; anisotropy is represented by unequal eigenvalues, and homogeneity is manifested by the constancy of the cumulants (Equations (9)–(11)) over the domain on which the field is defined.

4. Minkowski Tensors—Spherical Redshift-space Distortion

The plane-parallel limit reviewed in the previous section is an approximation where the observed patch of the density field is sufficiently distant from the observer and localized on the sky so that the line of sight can be approximately aligned with one of the Cartesian axes. A detailed description of this approximation can be found in Castorina & White (2018).

Now we generalize and calculate the MTs without the plane-parallel approximation. Since RSD acts along the line of sight, we choose to work with the spherical coordinate system with the observer at the origin. The radial and angular basis vectors in this system are denoted $\boldsymbol{e}_r$, $\boldsymbol{e}_\theta$, $\boldsymbol{e}_\phi$; and $\boldsymbol{e}_r$ is aligned with the line of sight. The RSD operator is spherically symmetric and applied to an otherwise isotropic and homogeneous Gaussian random field. Under the assumption that the average number density of tracer particles is constant over the manifold, the

relation between the density field in real (δ) and redshift ($\tilde{\delta}$) space is given by Hamilton (1997):

$$\tilde{\delta}(\boldsymbol{r}) = \left[1 + f\left(\frac{\partial^2}{\partial r^2} + \frac{2}{r}\frac{\partial}{\partial r}\right)\nabla^{-2}\right]\delta(\boldsymbol{r}), \qquad (20)$$

to linear order in the fields. Here f is the growth factor that we assume to be constant, neglecting its redshift dependence. The RSD operator in square brackets is now radial relative to a central observer located at $r = 0$. There is no longer a uniformly parallel line-of-sight vector over the entire manifold—the line of sight is now aligned with the radial basis vector $\boldsymbol{e}_r$. The redshift-space field is sensitive to this vector, because the tracer particles that are used to define $\tilde{\delta}$ are perturbed according to the component of their velocity parallel to the corresponding line-of-sight direction. The radial nature of the signal renders the redshift-space distorted field inhomogeneous, and the two-point correlation function of $\tilde{\delta}$ is no longer solely a function of the separation between two tracer particles, but now depends on the triangle formed by the observer and the two points. Translation invariance is broken, but the residual rotational symmetry around the observer and azimuthal symmetry about the line of sight persists.

4.1. Ensemble Average $\langle w_i^j \rangle$

The goal of this section is to derive the ensemble average of the tensor w_i^j for the field $\tilde{\delta}$ defined in Equation (20), in a spherical coordinate system. The first step is to derive the cumulants $\langle \tilde{\delta}^2 \rangle$, $\langle \tilde{\delta}\tilde{\delta}_i \rangle$, and $\langle \tilde{\delta}_i\tilde{\delta}^j \rangle$. The variance of the field $\langle \tilde{\delta}^2 \rangle$ is a scalar quantity and hence invariant under coordinate transformations, but $\langle \tilde{\delta}_i\tilde{\delta}^j \rangle$ is a rank (1, 1) tensor, and $\langle \tilde{\delta}\tilde{\delta}_i \rangle$ is a vector, both of which transform nontrivially. Spherical redshift-space two-point statistics have been extensively studied in the literature, and we direct the reader to Hamilton (1992), Hamilton & Culhane (1996), Zaroubi & Hoffman (1996), Szalay et al. (1998), Szapudi (2004), Shaw & Lewis (2008), Bonvin & Durrer (2011), Raccanelli et al. (2016), Yoo & Seljak (2014), Reimberg et al. (2016), Paul et al. (2022) and references therein for details.

Starting with the scalar cumulant, following Castorina & White (2018), we define the density field in terms of angular coefficients as

$$\tilde{\delta}(\boldsymbol{r}) = \sum_{\ell m} a_{\ell m}(r) Y_{\ell m}^*(\boldsymbol{e}_r). \qquad (21)$$

Then the two-point function is given by

$$\langle \tilde{\delta}(\boldsymbol{r}')\tilde{\delta}(\boldsymbol{r}) \rangle = \zeta(\boldsymbol{r}, \boldsymbol{r}') = \sum_{\ell m} \langle a_{\ell m}(r) a_{\ell m}(r') \rangle Y_{\ell m}(\boldsymbol{e}_r) Y_{\ell m}^*(\boldsymbol{e}_{r'}) \qquad (22)$$

$$= \sum_{\ell} \frac{2\ell + 1}{4\pi} C_\ell(r, r') \mathcal{L}_\ell(\boldsymbol{e}_r.\boldsymbol{e}_{r'}), \qquad (23)$$

where

$$C_\ell(r, r') = \frac{2}{\pi} \int dk k^2 P(k, R_G)\left[j_\ell(kr) \right.$$
$$- f\left(j''_\ell(kr) + \frac{2}{kr}j'_\ell(kr)\right)\right]$$
$$\times \left[j_\ell(kr') - f\left(j''_\ell(kr') + \frac{2}{kr'}j'_\ell(kr')\right)\right], \qquad (24)$$

where primes on the spherical Bessel function j_ℓ denote differentiation with respect to the argument kr, or kr' and $\mathcal{L}_\ell$ are Legendre polynomials. The cumulant is defined as the field correlation in the limit $\boldsymbol{r} \to \boldsymbol{r}'$, which is

$$\tilde{\sigma}_0^2 \equiv \langle \tilde{\delta}(\boldsymbol{r}')\tilde{\delta}(\boldsymbol{r}) \rangle|_{\boldsymbol{r}' \to \boldsymbol{r}} = \frac{1}{2\pi^2} \int dk k^2 P(k, R_G) \sum_{\ell=0}^{\infty} (2\ell + 1)$$
$$\times \left[j_\ell^2(kr) - 2fj_\ell(kr)j''_\ell(kr) + f^2[j''_\ell(kr)]^2 + \right.$$
$$\left. - \frac{4f}{kr}j_\ell(kr)j'_\ell(kr) + \frac{4f^2}{kr}j''_\ell(kr)j'_\ell(kr) + \frac{4f^2}{k^2r^2}[j'_\ell(kr)]^2\right],$$
$$= \frac{1}{2\pi^2} \int dk k^2 P(k, R_G)\left[1 + \frac{2}{3}f + \frac{1}{5}f^2\right]$$
$$+ \frac{4f^2}{3r^2}\frac{1}{2\pi^2} \int dk P(k, R_G), \qquad (25)$$

where we took the limit $\boldsymbol{r}' \to \boldsymbol{r}$ on the right-hand side and used the normalization of the Legendre polynomials $\mathcal{L}_\ell(\boldsymbol{e}_r.\boldsymbol{e}_r) = 1$. The first term on the right-hand side of Equation (25) is the cumulant in the plane-parallel limit. The second term is divergent as $r \to 0$ but falls off at large distances from the central observer. The divergent behavior at $r = 0$ is not physical, and can be subtracted via a suitable correction to the space distortion operator in Equation (20). Practically, cosmological data will always occupy a domain excluding the observer, and for computational purposes, we will excise the $r = 0$ point from the manifold in redshift space. Hence the manifold on which the RSD field $\tilde{\delta}$ is defined is not $\mathbb{R}^3$, but rather $\mathbb{S}^2 \times \mathbb{R}_{>0}$.

Similarly the radial and angular derivative cumulants can be calculated—

$$\langle \tilde{\delta}_r(\boldsymbol{r}')\tilde{\delta}^r(\boldsymbol{r}) \rangle|_{\boldsymbol{r}' \to \boldsymbol{r}} = \frac{1}{2\pi^2} \int dk k^4 P(k, R_G) \sum_{\ell=0}^{\infty} (2\ell + 1)$$
$$\times \left[[j'_\ell(kr)]^2 - 2fj'_\ell(kr)j'''_\ell(kr) + f^2[j'''_\ell(kr)]^2\right.$$
$$+ \frac{4f^2}{k^2r^2}j''_\ell(kr)j''_\ell(kr) + \frac{4f}{k^2r^2}j'_\ell(kr)j'_\ell(kr)$$
$$- \frac{4f^2}{k^2r^2}j'_\ell(kr)j'''_\ell(kr)$$
$$\left. + \frac{4f^2}{k^4r^4}j'_\ell(kr)j'_\ell(kr)\right]$$
$$= \frac{1}{2\pi^2} \int dk k^4 P(k, R_G)\left[\frac{1}{3} + \frac{2}{5}f + \frac{1}{7}f^2\right]$$
$$+ \frac{1}{2\pi^2 r^2} \int dk k^2 P(k, R_G)\left[\frac{4f}{3} + \frac{8f^2}{5}\right] +$$
$$+ \frac{1}{2\pi^2 r^4} \int dk P(k, R_G)\frac{4f^2}{3}, \qquad (26)$$

and

$$\langle \tilde{\delta}_{\phi}(\boldsymbol{r}') \tilde{\delta}^{\phi}(\boldsymbol{r}) \rangle|_{\boldsymbol{r}' \to \boldsymbol{r}} = \frac{1}{4\pi^2 r^2} \int dk k^2 P(k, R_G)$$

$$\times \sum_{\ell=0}^{\infty} \ell(\ell+1)(2\ell+1)$$

$$\times \left[j_{\ell}^2(kr) - 2f j_{\ell}(kr) j''_{\ell}(kr) + f^2 j''_{\ell}(kr) j''_{\ell}(kr) + \right.$$

$$- \frac{4f}{kr} j_{\ell}(kr) j'_{\ell}(kr) + \frac{4f^2}{kr} j''_{\ell}(kr) j'_{\ell}(kr)$$

$$\left. + \frac{4f^2}{k^2 r^2} j'_{\ell}(kr) j'_{\ell}(kr) \right]$$

$$= \frac{1}{2\pi^2} \int dk k^4 P(k, R_G) \left[\frac{1}{3} + \frac{2}{15} f + \frac{1}{35} f^2 \right]$$

$$+ \frac{1}{2\pi^2 r^2} \int dk k^2 P(k, R_G) \left[-\frac{4}{3} f + \frac{8}{15} f^2 \right]$$

$$+ \frac{1}{2\pi^2 r^4} \int dk P(k, R_G) \frac{4f^2}{3}; \quad (27)$$

$$\langle \tilde{\delta}_{\theta}(\boldsymbol{r}') \tilde{\delta}^{\theta}(\boldsymbol{r}) \rangle|_{\boldsymbol{r}' \to \boldsymbol{r}} = \frac{1}{2\pi^2} \int dk k^4 P(k, R_G)$$

$$\times \left[\frac{1}{3} + \frac{2}{15} f + \frac{1}{35} f^2 \right]$$

$$+ \frac{1}{2\pi^2 r^2} \int dk k^2 P(k, R_G) \left[-\frac{4}{3} f + \frac{8}{15} f^2 \right]$$

$$+ \frac{1}{2\pi^2 r^4} \int dk P(k, R_G) \frac{4f^2}{3}. \quad (28)$$

The cross covariance terms are 0 in this coordinate system—for example

$$\langle \tilde{\delta}_r(\boldsymbol{r}') \tilde{\delta}^{\phi}(\boldsymbol{r}) \rangle|_{\boldsymbol{r}' \to \boldsymbol{r}} = \frac{2}{\pi} \int dk k^3 P(k, R_G) \sum_{\ell=0}^{\infty}$$

$$j_{\ell}(kr) j'_{\ell}(kr) \sum_{m=-\ell}^{\ell} (im) Y_{\ell m}(\boldsymbol{e}_r) Y_{\ell m}^*(\boldsymbol{e}_r) = 0. \quad (29)$$

Similarly

$$\langle \tilde{\delta}_{\theta}(\boldsymbol{r}') \tilde{\delta}^{\phi}(\boldsymbol{r}) \rangle|_{\boldsymbol{r}' \to \boldsymbol{r}} = \langle \tilde{\delta}_r(\boldsymbol{r}') \tilde{\delta}^{\theta}(\boldsymbol{r}) \rangle|_{\boldsymbol{r}' \to \boldsymbol{r}} = 0. \quad (30)$$

Hence in this coordinate system, the gradient cumulant tensor $\langle \tilde{\delta}_i \tilde{\delta}^j \rangle$ is diagonal. There is an additional correlation not present for a homogeneous field—the vector $\langle \tilde{\delta} \tilde{\delta}_i \rangle$ has a single nonzero component

$$\langle \tilde{\delta}(\boldsymbol{r}') \tilde{\delta}_r(\boldsymbol{r}) \rangle|_{\boldsymbol{r}' \to \boldsymbol{r}} = \frac{1}{2\pi^2} \int dk k^3 P(k, R_G) \sum_{\ell} (2\ell+1)$$

$$\times \left[j_{\ell}(kr) - f \left(j''_{\ell}(kr) + \frac{2}{kr} j'_{\ell}(kr) \right) \right]$$

$$\times \left[j'_{\ell}(kr) - f \left(j'''_{\ell}(kr) + \frac{2}{kr} j''_{\ell}(kr) - \frac{2}{k^2 r^2} j'_{\ell}(kr) \right) \right]$$

$$= -\frac{4f^2}{3r^3} \frac{1}{2\pi^2} \int dk P(k, R_G). \quad (31)$$

There are two crucial differences between this scenario and the previous plane-parallel calculation in Appleby et al. (2019)—the cumulants are now explicitly functions of the position on

the manifold at which they are estimated, and they are no longer defined over $\mathbb{R}^3$ because we excise the $r = 0$ point. Both are consequences of the inhomogeneous nature of the RSD signal. In each of the cumulants (Equations (25)–(28)), the first terms on the right-hand sides correspond to the plane-parallel limit, and the remaining terms are corrections that are fractionally suppressed by $\sigma_0^2/(\sigma_1^2 r^2)$ and $\sigma_{-1}^2/(\sigma_1^2 r^4)$ at large distances from the observer. Similarly the vector $\langle \tilde{\delta} \tilde{\delta}_i \rangle$ has asymptotic behavior $\langle \tilde{\delta} \tilde{\delta}_i \rangle \to 0$ as $\sigma_{-1}^2/(\sigma_0 \sigma_1 r^3) \to 0$. Hence, at large distances from the observer, the cumulants approach their constant, plane-parallel limits. The ensemble average, being defined at a point on the manifold, is independent of the volume on which the field is defined, and the approach to the plane-parallel limit is sensitive only to the ratio of the R_G-dependent cumulants and radial distance r. The volume occupied by the field is important when extracting the volume average from the data.

To quantify the departure of the cumulants from the plane-parallel limit, we numerically evaluate Equation (26) for a typical cold dark matter density field in the linearized limit. Taking cosmological parameters from Table 1, we generate a linear ΛCDM matter power spectrum $P(k, R_G)$ at $z = 0$, and we use this and $f \simeq \Omega_m^{\gamma}$, $\gamma = 6/11$ to numerically reconstruct the plane-parallel limit $\tilde{\sigma}_{r,\parallel}^2$ and radial-dependent correction Δ_r^2 to the cumulant, $\langle \tilde{\delta}_r(\boldsymbol{r}) \tilde{\delta}^r(\boldsymbol{r}) \rangle = \tilde{\sigma}_{r,\parallel}^2 + \Delta_r^2$, defined as

$$\tilde{\sigma}_{r,\parallel}^2 \equiv \frac{1}{2\pi^2} \int dk k^4 P(k, R_G) \left[\frac{1}{3} + \frac{2}{5} f + \frac{1}{7} f^2 \right]; \quad (32)$$

$$\Delta_r^2(r) \equiv \frac{1}{2\pi^2 r^2} \int dk k^2 P(k, R_G) \left[\frac{4f}{3} + \frac{8f^2}{5} \right]$$

$$+ \frac{1}{2\pi^2 r^4} \int dk P(k, R_G) \frac{4f^2}{3}. \quad (33)$$

In the left panel of Figure 1, we present the dimensionless fraction $\Delta_r^2 / \tilde{\sigma}_{r,\parallel}^2$ as a function of comoving distance r from an observer at $r = 0$ using the standard ΛCDM distance–redshift relation with parameters given in Table 1. We select Gaussian smoothing scales $R_G = 20, 40$ Mpc (blue, green lines). We only present $\langle \tilde{\delta}_r(\boldsymbol{r}) \tilde{\delta}^r(\boldsymbol{r}) \rangle$, as this is representative of the other cumulants. In the right panel, we present the same quantity as a function of dimensionless ratio r/R_G.

The figure shows that the coordinate dependent corrections to the cumulant are negligible for $r \gg R_G$, and that for cosmological density fields that occupy a redshift domain $r > \mathcal{O}(10 R_G)$ the radial cumulant is practically equal to its plane-parallel limit, $\langle \tilde{\delta}_r(\boldsymbol{r}) \tilde{\delta}^r(\boldsymbol{r}) \rangle \simeq \tilde{\sigma}_{r,\parallel}^2$. Conversely, for $r \lesssim R_G$, the Δ_r^2 term is the dominant contribution to the cumulant, which is strongly position dependent. In this regime,
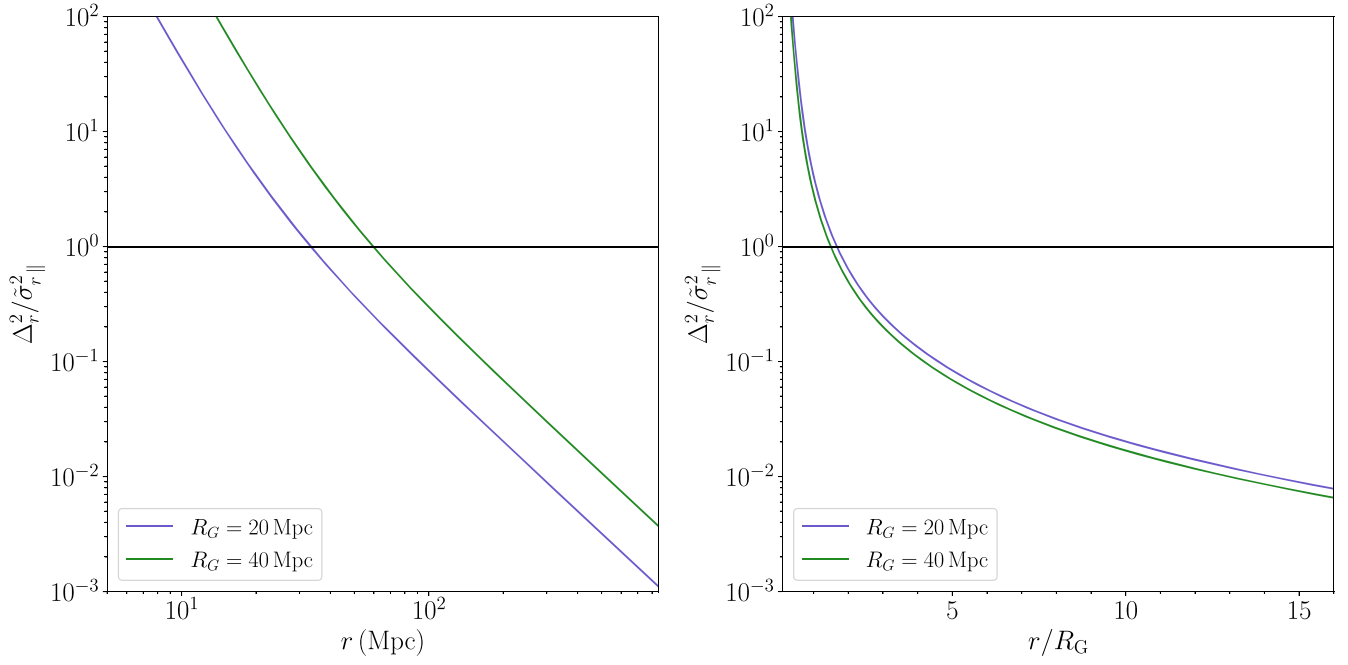
Figure 1. Fractional correction to the radial cumulant $\tilde{\sigma}_r^2$ due to the inhomogeneous contribution $\Delta_r^2(r)$, relative to its plane-parallel limit $\tilde{\sigma}_{r,\parallel}^2$. Blue and/or green lines correspond to smoothing scales $R_G = 20, 40$ Mpc respectively. We present $\Delta_r^2(r)/\tilde{\sigma}_r^2$ as a function of comoving distance from observer (left panel) and ratio of comoving distance and smoothing scale (right panel).

the cumulants grow without bound as $r \to 0$, so there is always a region for which the field $\tilde{\delta}$ cannot be considered perturbatively small. However, the region $r \lesssim R_G$ is not typically utilized in any cosmological scale density field reconstruction, and the plane-parallel limit of the cumulants is very accurate for our purposes.

After calculating the cumulants $\langle \tilde{\delta}_i \tilde{\delta}^j \rangle$, $\langle \tilde{\delta} \tilde{\delta}_i \rangle$, $\langle \tilde{\delta}^2 \rangle$, we can now estimate the ensemble average $\langle w_i^j \rangle$ —

$$\langle w_i{}^j \rangle = \frac{1}{6} \int \Phi(X, \Sigma(r)) \frac{\tilde{\delta}_i \tilde{\delta}^j}{|\nabla \tilde{\delta}|} \delta_D(\tilde{\delta} - \delta_t) dX \qquad (34)$$

where $\Phi(X, \Sigma(r))$ is the probability distribution of the variables X. The array X denotes any combination of the stochastic fields $(\tilde{\delta}, \tilde{\delta}_r, \tilde{\delta}_\theta, \tilde{\delta}_\phi)$ to which w_i^j is sensitive. Σ is a square matrix whose dimension is given by the number of components of X.

We use the fact that $\tilde{\delta}_\theta$ and $\tilde{\delta}_\phi$ are uncorrelated with $\tilde{\delta}$ and $\tilde{\delta}_r$ and one another, and their variances are equal as given by Equations (27), (28). Furthermore, if the density field is statistically isotropic on the two-sphere, it suffices to calculate $\langle w_\theta^\theta + w_\phi^\phi \rangle$, and then halve this value to obtain the individual elements. To estimate $\langle w_\theta^\theta + w_\phi^\phi \rangle$ and $\langle w_r^r \rangle$, we can use the variables $X = (\tilde{\delta}, \tilde{\delta}_r, y)$, where $y = \sqrt{\tilde{\delta}_\theta \tilde{\delta}^\theta + \tilde{\delta}_\phi \tilde{\delta}^\phi}$, where $\tilde{\delta}_\phi \tilde{\delta}^\phi$ and $\tilde{\delta}_\theta \tilde{\delta}^\theta$ are given by Equations (27) and (28) respectively. The random field y is Rayleigh distributed and uncorrelated with $\tilde{\delta}$ and $\tilde{\delta}_r$. The fields $\tilde{\delta}$ and $\tilde{\delta}_r$ are Gaussian random variables with nonzero correlations:

$$\hat{\Sigma}(r) \equiv \begin{pmatrix} \langle \tilde{\delta}^2 \rangle & \langle \tilde{\delta} \tilde{\delta}_r \rangle \\ \langle \tilde{\delta} \tilde{\delta}_r \rangle & \langle \tilde{\delta}_r \tilde{\delta}^r \rangle \end{pmatrix}. \qquad (35)$$

Each term in $\hat{\Sigma}$ is nonzero and a function of r, but in the limit $r \gg \sigma_0/\sigma_1$, and $r \gg \sqrt{\sigma_1/\sigma_{-1}}$, Σ approaches a diagonal form with constant components—the plane-parallel limit of Appleby et al. (2019). In the same limit, the variance σ_y^2 becomes

independent of the radial coordinate. Defining $\boldsymbol{d} = (\tilde{\delta}, \tilde{\delta}_r)$, $X = (\boldsymbol{d}, y)$, and the probability distribution is

$$\Phi(\boldsymbol{d}, y, \Sigma(r)) = \frac{y}{\sigma_y^2 \sqrt{(2\pi)^2 |\hat{\Sigma}|}} \exp\left[-\frac{1}{2} \boldsymbol{d}^T \hat{\Sigma}^{-1} \boldsymbol{d} - \frac{y^2}{2\sigma_y^2} \right],$$
$$(36)$$

where $\sigma_y^2 = \langle \tilde{\delta}_\theta \tilde{\delta}^\theta \rangle = \langle \tilde{\delta}_\phi \tilde{\delta}^\phi \rangle$. Although we cannot perform the integral in Equation (34) analytically, $\langle w_i^j \rangle$ can be numerically estimated for any r. In the regime $r^2 \gg \sigma_0^2/\sigma_1^2$, and $r^4 \gg \sigma_{-1}^2/\sigma_1^2$, we can use the plane-parallel limit calculated in Appleby et al. (2019) as an excellent approximation.

In Figure 2, we present the ensemble average (Equation (34)) using the probability distribution (Equation (36)) for fixed $R_G = 20$ Mpc, using the radially dependent cumulants in $\hat{\Sigma}(r)$ and $\sigma_y^2(r)$. The yellow, blue, and green curves correspond to the value of the ensemble average at $r = 10, 25, 50$ Mpc respectively, and the solid and dashed curves are the (r, r) and (θ, θ) components. The (ϕ, ϕ) components are always equal to the (θ, θ) element, and so they are not plotted. The gray lines correspond to the plane-parallel limit of the ensemble average, obtained by taking r to be some arbitrarily high value $r = 10^3$ Mpc. For $r < R_G$, the ensemble average significantly departs from the standard Gaussian expectation value (see yellow, blue curves). This is due to the r dependent terms in the cumulants dominating for $r < R_G$, and also the shape change in the (r, r) component is due to the cross correlation contribution $\langle \tilde{\delta} \tilde{\delta}_r \rangle \neq 0$. For $r > R_G$, the components approach the plane-parallel limit (see green curves).

The shape of the $\langle w_i^j \rangle$ curves depend on the correlation properties of the field. When $\langle \delta \delta_i \rangle = 0$, the components of $\langle w_i^j \rangle$ possess the well-known ν functional dependence $e^{-\nu^2/2}$. Any correlation between the field and its gradient will
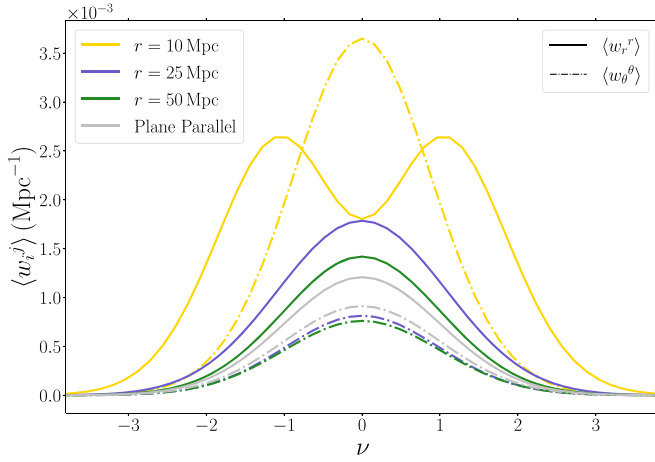
7

Figure 2. The ensemble average (Equation (34)) for the spherically redshift-space distorted field, evaluated at distance $r = 10, 25, 50$ Mpc from the central observer (yellow, blue, green lines), as a function of constant normalized threshold $\nu = \delta_t/\tilde{\sigma}_0$. We also present an example with very large separation from the observer $r = 10^3$ Mpc, which we label as "Plane Parallel" (gray lines).

modify the shape of these statistics, even for a Gaussian random field. Practically, it would not be feasible to extract the extremely nonstandard ν dependence presented in Figure 2 for $r < R_G$ from large-scale structure catalogs, because we measure the volume average $\bar{w}_i{}^j$, and for $r < R_G$, the volume is insufficient to obtain the fair sample required to estimate $\langle w_i^j \rangle$. Still, we can potentially probe small perturbations to the shape of the Minkowski functionals and tensors arising from the $\langle \delta \delta_i \rangle$ field correlation.

4.2. Volume Average $\bar{w}_i^j$

Next we consider what is actually extracted from cosmological data—the volume average of w_i^j. We assume that the continuous field $\tilde{\delta}$ has been sampled at a finite set of points, specifically we take $\tilde{\delta}$ evaluated on a Cartesian grid in a cubic volume. The volume of the cube is L^3 Mpc^3, and each pixel occupies volume Δ^3 Mpc^3. We denote a discretized field with subscript $\{...\}$ brackets to denote pixel dependence, so $\tilde{\delta}_{\{m,n,p\}}$ is the value of the field in the m, n, p pixel in (x, y, z) coordinates. We define the Cartesian basis vectors as $\boldsymbol{e}_x, \boldsymbol{e}_y, \boldsymbol{e}_z$, and spherical basis vectors $\boldsymbol{e}_r, \boldsymbol{e}_\theta, \boldsymbol{e}_\phi$ in a coordinate system with respect to an observer located at the center of the cube. At each grid point, we construct the gradient of the field in Cartesian coordinates using a second-order accurate finite difference scheme. Then w_i^j at each point on the grid is given by

$$w_i{}^j{}_{\{m,n,p\}} = \frac{1}{6} \frac{\tilde{\delta}_{i\{m,n,p\}} \tilde{\delta}^j{}_{\{m,n,p\}}}{|\nabla \tilde{\delta}_{\{m,n,p\}}|} \delta_D(\tilde{\delta}_{\{m,n,p\}} - \delta_t), \quad (37)$$

where the Dirac delta function is also discretized (Schmalzing & Buchert 1997):

$$\delta_D(\tilde{\delta}_{\{m,n,p\}} - \delta_t) = \begin{cases} \epsilon^{-1} & \text{if} \quad |\tilde{\delta}_{\{m,n,p\}} - \delta_t| < \epsilon/2 \\ 0 & \text{Otherwise.} \end{cases} \quad (38)$$

ϵ is a small parameter that we fix as $\epsilon = 10^{-2}$ in what follows. There is a discretization error that comes with this approximation (Lim & Simon 2012; Chingangbam & Yogendran 2017), but we neglect this subtlety. The function $\delta_D(\tilde{\delta}_{\{m,n,p\}} - \delta_t)$ selects a subset of pixels of roughly equal field value, which are the points on $\mathbb{M}$ at which we sample the vector

field $\tilde{\delta}_{i\{m,n,p\}}$ for each threshold δ_t. Since the gradient of the field $\tilde{\delta}_i$ is approximately uncorrelated with $\tilde{\delta}$ point-wise on the manifold, this sampling generates an unbiased estimate of the underlying vector field $\tilde{\delta}_i$ for every δ_t. The only caveat is that, in spherical redshift space, $\tilde{\delta}_r$ is weakly correlated with $\tilde{\delta}$, but the correlation is negligible for $r^4 \gg \sigma_{-1}^2/\sigma_1^2$. The quantity $w_{\{m,n,p\}}^j$ is a tensor evaluated at a particular point on the manifold (specified by the $\{m,n,p\}$ pixel), and $\bar{w}_i{}^j$ is their volume average. In Figure 14, Appendix C, we present an example of a point distribution data set, the corresponding smoothed field, and the discretized delta function approach to selecting pixels of particular threshold value.

The concept of a volume average of non-Cartesian tensors defined at different points on a manifold is ambiguous. To proceed, we should define a fiducial pixel $\{a, b, c\}$ at which we take the volume average, and a choice of path by which we transport each $w_{i\{m,n,p\}}^j$ to $\{a, b, c\}$. We write the volume average as

$$\bar{w}_i{}^j(\gamma, a, b, c) = \frac{1}{6V} \sum_{m,n,p} \Delta^3$$

$$\delta_D(\tilde{\delta}_{\{m,n,p\}} - \delta_t) \frac{{}^\gamma\tilde{\delta}_{i\{m,n,p\}} {}^\gamma\tilde{\delta}^j{}_{\{m,n,p\}}}{|\nabla \tilde{\delta}_{\{m,n,p\}}|}, \quad (39)$$

where the γ superscript ${}^\gamma\tilde{\delta}_i$ denotes the transport of $\tilde{\delta}_i$ from $\{m, n, p\}$ to $\{a, b, c\}$ along a path γ, and

$$V = \sum_{m,n,p} \Delta^3. \quad (40)$$

We do not use all pixels in the cubic volume, but rather $\sum_{m,n,p}$ represents all pixels that lie in some radial range $r_{\min} \leqslant r \leqslant r_{\max}$, where $r_{\min} > R_G$, and $r_{\max} < L/2$ are selected to ensure that we cut pixels close to the central observer and in the vicinity of the boundary of the box.

The choice of path γ is completely arbitrary. However, the manifold on which the field is defined is $\mathbb{S}^2 \times \mathbb{R}_{>0}$, which is geodesically incomplete with respect to Euclidean paths. Since we are adopting a spherical coordinate system and anticipate a preferred signal in the radial direction, it behooves us to select a transport that preserves the radial basis vector. A natural choice that achieves this is great arc transport on the two-sphere from the angular location of $\{m, n, p\}$ to $\{a, b, c\}$ followed by a radial translation to the same distance from the central observer. Great arc transport from $\{m, n, p\}$ to $\{a, b, c\}$ rotates the spherical basis vectors $\boldsymbol{e}_r \rightarrow \boldsymbol{e}'_r, \boldsymbol{e}_\theta \rightarrow \boldsymbol{e}'_\theta, \boldsymbol{e}_\phi \rightarrow \boldsymbol{e}'_\phi$, such that $\boldsymbol{e}'_r = \boldsymbol{e}_r$, but $\boldsymbol{e}'_\theta$ and $\boldsymbol{e}'_\phi$ become mixed relative to $\boldsymbol{e}_\theta$, $\boldsymbol{e}_\phi$.[7] The mixing of spherical components is unimportant, because we are assuming that the field is isotropic on $\mathbb{S}^2$. We explicitly present the rotation of the spherical basis vectors—relative to great arc tangents—in Appendix B. For both the plane-parallel and spherical redshift-space distorted fields, the field is assumed to be isotropic on the submanifold perpendicular to the line of sight—$\mathbb{R}^2$ relative to $\boldsymbol{e}_z$ and $\mathbb{S}^2$ relative to $\boldsymbol{e}_r$ respectively.

To perform this transport for all pixels that satisfy $\delta_D(\tilde{\delta}_{\{m,n,p\}} - \delta_t) \neq 0$, we define $\hat{\boldsymbol{T}}_1$ and $\hat{\boldsymbol{T}}_2$ as unit vectors

---

[7] Parallel transport along geodesics on $\mathbb{S}^2$ preserves the orientation of the tangent space relative to the tangent vector of the transport. The mixing described here arises due to the fact that the angle subtending a great arc tangent vector and the basis vectors $\boldsymbol{e}_\theta, \boldsymbol{e}_\phi$ varies continuously along the path.

pointing to pixels $\{m, n, p\}$ and $\{a, b, c\}$ from the *observer* at $r = 0$, and rotate the vector $\tilde{\delta}_{i\,\{m,n,p\}}$ by angle $\cos\theta = \hat{\boldsymbol{T}}_1 \cdot \hat{\boldsymbol{T}}_2$, about the axis defined by $\hat{\boldsymbol{T}}_1 \times \hat{\boldsymbol{T}}_2$. Such a rotation can be used to describe great arc transport. The second stage of transport, along $\boldsymbol{e}_r$, is trivial and undertaken implicitly. Finally the transported, Cartesian gradient $\tilde{\delta}'_{i\,\{m,n,p\}}$, now defined at $\{a, b, c\}$, is converted into the spherical basis via a coordinate transformation. Note that we used a Cartesian basis to define $\tilde{\delta}_i$ and performed a coordinate transformation as a final step, but one could instead define $\tilde{\delta}_i$ in a spherical basis then rotate from $\{m, n, p\}$ to $\{a, b, c\}$. The final result will not depend on the ordering of these operations.

In Figure 3, we present a schematic image of the vectors associated with the transport scheme. The tan and red vectors are the vectors pointing to $\hat{\boldsymbol{T}}_1$ and $\hat{\boldsymbol{T}}_2$ respectively. The purple vector is $\tilde{\delta}_i$, at point $\{m, n, p\}$. The blue and/or black lines denote the great arc and Euclidean paths to point $\{a, b, c\}$, and the violet/green vectors denote $\tilde{\delta}_i$ after these respective transports. The green vector is parallel to the purple; the violet and purple vectors are both parallel to the tangent vector to the blue curve. In this work, we adopt great arc transport, which transports the purple to the violet vector at $\{a, b, c\}$.

If we used Euclidean paths to transport $\tilde{\delta}_i$ to a common point on the manifold (ignoring the geodesic incompleteness), then we would obtain a completely different result. In this case, all three spherical basis vectors $\boldsymbol{e}_r$, $\boldsymbol{e}_\theta$, $\boldsymbol{e}_\phi$ would mix, and $\bar{w}_i{}^j$ would depend entirely on the volume over which the field is defined.

The fact that the choice of transport affects the volume average is troubling, because the ensemble average is defined at a point on the manifold and requires no notion of transport. However, we expect that our choice is appropriate for the very specific physical scenario considered in this work. With our path selection, the radial basis vector is preserved, and although the angular derivatives become mixed, we are working with a field that is isotropic on $\mathbb{S}^2$. Other choices of path could be used instead—for example transport along lines of latitude and longitude. This choice is not angle preserving—lines of latitude are not generally geodesics. Ultimately there is no unique path definition, but for a field that is isotropic on $\mathbb{S}^2$, these details are not important. Also the point on $\mathbb{S}^2$ at which we take the average will not impact the volume average for an idealized field that is isotropic on $\mathbb{S}^2$. Anisotropic fields on $\mathbb{S}^2$ will be considered elsewhere, as many of these subtleties are likely to become problematic in the absence of this symmetry.

We would like to equate the volume and ensemble averages of w_i^j, defined in Equations (39) and (34) respectively.[8] As justification, we can appeal to the weak law of large numbers; for a sequence of identically distributed variables X_n, we define an average

$$\bar{X} = \frac{1}{N}\sum_{n=1}^{N} X_n. \tag{41}$$

Then if the covariance between variables (X_n, X_{n+m}) asymptotes to 0 as $m \to \infty$, the sample mean $\bar{X}$ in Equation (41) approaches the underlying expectation value $E(X)$ in the limit $N \to \infty$. In our example, the summed variables are the
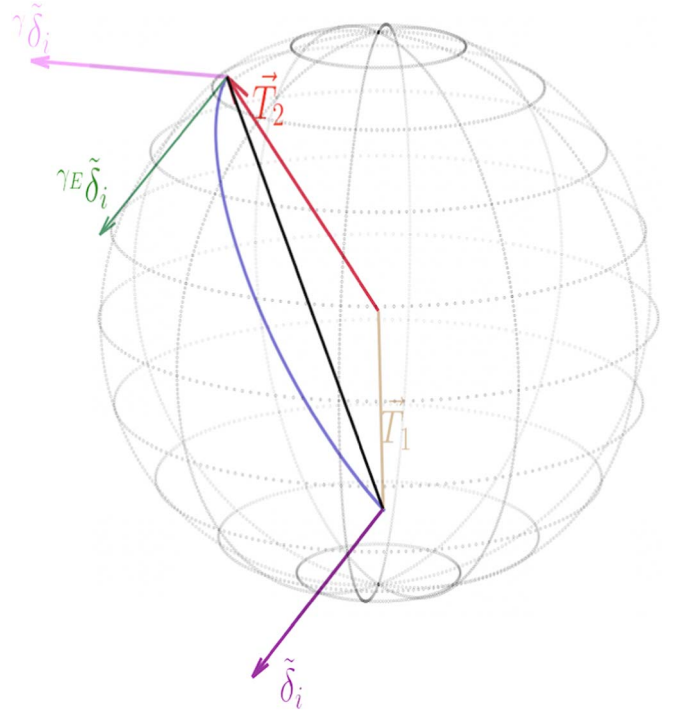

Figure 3. Figure showing the parallel transport of the vector $\tilde{\delta}_i$ from point $\{m, n, p\}$ (purple vector) to $\{a, b, c\}$, using great arcs on the two-sphere (violet vector) and Euclidean transport (green vector).

combination on the right-hand side of Equation (39). As we take the volume $V \to \infty$, we expect that the pixels will provide a fair sample, and the correlation functions of $\tilde{\delta}$ and its gradient satisfy $\zeta(r) \to 0$ as $r \to \infty$. This suggests that the ensemble and sample averages will converge, but in realistic scenarios, we deal with finite volumes, and furthermore the fields $\tilde{\delta}$, $\tilde{\delta}_i$ are non-Gaussian in the low redshift universe. It is not clear that the sample and ensemble averages converge when higher point correlations are present, and if so how quickly they do as the volume increases (Watts & Coles 2003). With our choice of transport, we do not expect the volume average to be sensitive to the point on the sphere at which we take the average, and we will take the density fields located at $r \gg R_G$, so the radial dependence of the cumulants should be irrelevant. We therefore expect that, for this particular physical scenario, our choice of coordinate system and transport will allow us to use the approximation $\bar{w}_i{}^j \simeq \langle w_i{}^j \rangle$. At precisely what scale the plane-parallel approximation and ergodicity can be reasonably applied depends on the radial distance between the observer and the data, and the smoothing scale R_G used. From Figure 1 (right panel), we expect that corrections to the plane-parallel limit become subpercent at radial distances equal to approximately ten smoothing lengths. This implies that for cosmological large-scale structure data (Alam et al. 2015) the plane-parallel approximation should be accurate to more than 1%, as these catalogs are hundreds of Megaparsecs from the observer, and we typically smooth on scales $\sim\mathcal{O}(10\,\mathrm{Mpc})$. However, small departures from the plane-parallel limit should be observable in local large-scale structure catalogs at redshifts $z < 0.1$ (Abazajian et al. 2009). Measuring these deviations is a direction of future study.

---

[8] Since we measure $\bar{w}_i{}^j \equiv W_1^{0,2}$ from a cosmological density field, we should not compare the measurement to the ensemble average of the Minkowski tensor $\langle W_1^{0,2} \rangle$ but rather $\langle w_i{}^j \rangle$. When the field is statistically homogeneous, we can write $\langle w_i{}^j \rangle = \langle W_1^{0,2} \rangle$, and there is no distinction to be made.

We confirm the accuracy of the plane-parallel approximation numerically in Section 6. However, before moving on to the numerics, we present a counter example in Section 5 for which the notion of ergodicity (even approximate) fails completely.

5. Spherical Redshift-space, Cartesian Coordinate System

In this section, we calculate the cumulants of the spherically redshift-space distorted field in Cartesian coordinates (x, y, z), following the methodology of Castorina & White (2018). The calculation is extremely tedious, and we simply state some important steps and the results in the main body of the text. The density field in redshift space $\tilde{\delta}(\boldsymbol{r})$ can be written in terms of its real-space counterpart $\delta(\boldsymbol{r})$ via

$$\tilde{\delta}(\boldsymbol{r}) = \left(1 + \frac{f}{3}\right) \int \frac{d^3k}{2\pi^3} \mathcal{L}_0(\hat{k} \cdot \boldsymbol{e}_r) e^{i\boldsymbol{k}\cdot\boldsymbol{r}} \delta(\boldsymbol{k}) + \frac{2f}{r}$$
$$\times \int \frac{d^3k}{2\pi^3} \frac{\mathcal{L}_1(\hat{k} \cdot \boldsymbol{e}_r)}{ik} e^{i\boldsymbol{k}\cdot\boldsymbol{r}} \delta(\boldsymbol{k}) + \frac{2f}{3} \int \frac{d^3k}{2\pi^3} \mathcal{L}_2(\hat{k} \cdot \boldsymbol{e}_r) e^{i\boldsymbol{k}\cdot\boldsymbol{r}} \delta(\boldsymbol{k}),$$
$$(42)$$

where $\mathcal{L}_\ell$s are the Legendre polynomials.

We express $\boldsymbol{k}$ as $k_x \boldsymbol{e}_x + k_y \boldsymbol{e}_y + k_z \boldsymbol{e}_z$ in Cartesian coordinates. The differentiation of the first term on the right-hand side in Equation (42) with respect to x gives

$$\left(1 + \frac{f}{3}\right) \int \frac{d^3k}{2\pi^3} \frac{\partial}{\partial x} \mathcal{L}_0(\hat{k} \cdot \boldsymbol{e}_r) e^{i\boldsymbol{k}\cdot\boldsymbol{r}} \delta(\boldsymbol{k})$$
$$= \left(1 + \frac{f}{3}\right) \int \frac{d^3k}{2\pi^3} \delta(\boldsymbol{k}) \frac{\partial}{\partial x} e^{i\boldsymbol{k}\cdot\boldsymbol{r}}$$
$$= \left(1 + \frac{f}{3}\right) \int \frac{d^3k}{2\pi^3} (ik \sin\theta \cos\phi) e^{i\boldsymbol{k}\cdot\boldsymbol{r}} \delta(\boldsymbol{k}). \qquad (43)$$

We treat the other terms in the right-hand side of Equation (42) in a similar way and substitute the results into $\left\langle \frac{\partial}{\partial x}\tilde{\delta}(\boldsymbol{r})\frac{\partial}{\partial x}\tilde{\delta}(\boldsymbol{r}') \right\rangle\Big|_{\boldsymbol{r}'\to\boldsymbol{r}}$. We then use the relation (Equation C1), and $\mathcal{L}(\boldsymbol{e}_x \cdot \boldsymbol{e}_x) = 1$, along with the result

$$\langle \delta(\boldsymbol{k_1})\delta(\boldsymbol{k_2}) \rangle = (2\pi)^3 \delta_D^{(3)}(\boldsymbol{k_1} + \boldsymbol{k_2}) P(k), \qquad (44)$$

to get

$$\left\langle \frac{\partial}{\partial x}\tilde{\delta}(\boldsymbol{r})\frac{\partial}{\partial x'}\tilde{\delta}(\boldsymbol{r}') \right\rangle\Bigg|_{\boldsymbol{r}'\to\boldsymbol{r}} = \frac{4f^2}{3r^4} \int \frac{dkP(k, R_G)}{2\pi^2}$$
$$+ \left[\frac{4f}{3r^4}(2x^2 - r^2) + \frac{4f^2}{5r^4}(r^2 + x^2)\right] \int \frac{k^2 dkP(k, R_G)}{2\pi^2}$$
$$+ \left[\frac{1}{3} + \frac{2f}{15r^2}(r^2 + 2x^2) + \frac{f^2}{35r^2}(r^2 + 4x^2)\right]$$
$$\times \int \frac{k^4 dkP(k, R_G)}{2\pi^2}.$$
$$(45)$$

Similarly,

$$\left\langle \frac{\partial}{\partial y}\tilde{\delta}(\boldsymbol{r})\frac{\partial}{\partial y'}\tilde{\delta}(\boldsymbol{r}') \right\rangle\Bigg|_{\boldsymbol{r}'\to\boldsymbol{r}} = \frac{4f^2}{3r^4} \int \frac{dkP(k, R_G)}{2\pi^2}$$
$$+ \left[\frac{4f}{3r^4}(2y^2 - r^2) + \frac{4f^2}{5r^4}(r^2 + y^2)\right] \int \frac{k^2 dkP(k, R_G)}{2\pi^2}$$
$$+ \left[\frac{1}{3} + \frac{2f}{15r^2}(r^2 + 2y^2) + \frac{f^2}{35r^2}(r^2 + 4y^2)\right]$$
$$\times \int \frac{k^4 dkP(k, R_G)}{2\pi^2}, \qquad (46)$$

$$\left\langle \frac{\partial}{\partial z}\tilde{\delta}(\boldsymbol{r})\frac{\partial}{\partial z'}\tilde{\delta}(\boldsymbol{r}') \right\rangle\Bigg|_{\boldsymbol{r}'\to\boldsymbol{r}} = \frac{4f^2}{3r^4} \int \frac{dkP(k, R_G)}{2\pi^2}$$
$$+ \left[\frac{4f}{3r^4}(2z^2 - r^2) + \frac{4f^2}{5r^4}(r^2 + z^2)\right] \int \frac{k^2 dkP(k, R_G)}{2\pi^2}$$
$$+ \left[\frac{1}{3} + \frac{2f}{15r^2}(r^2 + 2z^2) + \frac{f^2}{35r^2}(r^2 + 4z^2)\right]$$
$$\times \int \frac{k^4 dkP(k, R_G)}{2\pi^2}, \qquad (47)$$

$$\left\langle \frac{\partial}{\partial x}\tilde{\delta}(\boldsymbol{r})\frac{\partial}{\partial y'}\tilde{\delta}(\boldsymbol{r}') \right\rangle\Bigg|_{\boldsymbol{r}'\to\boldsymbol{r}} = \left(\frac{8f}{3} + \frac{4f^2}{5}\right)\frac{xy}{r^4} \int \frac{k^2 dkP(k, R_G)}{2\pi^2}$$
$$+ \left(\frac{4f}{15} + \frac{4f^2}{35}\right)\frac{xy}{r^2} \int \frac{k^4 dkP(k, R_G)}{2\pi^2}, \qquad (48)$$

$$\left\langle \frac{\partial}{\partial x}\tilde{\delta}(\boldsymbol{r})\frac{\partial}{\partial z'}\tilde{\delta}(\boldsymbol{r}') \right\rangle\Bigg|_{\boldsymbol{r}'\to\boldsymbol{r}} = \left(\frac{8f}{3} + \frac{4f^2}{5}\right)\frac{xz}{r^4} \int \frac{k^2 dkP(k, R_G)}{2\pi^2}$$
$$+ \left(\frac{4f}{15} + \frac{4f^2}{35}\right)\frac{xz}{r^2} \int \frac{k^4 dkP(k, R_G)}{2\pi^2}. \qquad (49)$$

In this coordinate system, the cumulant tensor $\langle \tilde{\delta}_i \tilde{\delta}^j \rangle$ is not diagonal. We visualize the Cartesian cumulants in Figure 4. We smooth the power spectrum with a Gaussian kernel with scale $R_G = 20$ Mpc, select a fixed radial distance $r = 200$ Mpc from the central observer, and present Mollweide projections of the dimensionless quantity $\langle \tilde{\delta}_i \tilde{\delta}^j \rangle / \sigma_1^2$ on the sphere. The top row panels show the diagonal (x, x), (y, y), and (z, z) components (left to right), while the bottom row panels show (x, y), (x, z), and (y, z) components (left to right). The diagonal elements present a series of dipoles on the sphere, and the off-diagonal elements are quadrupolar. All elements are generically nonzero and vary significantly with spatial position. This is in contrast with the cumulants in a spherical coordinate system, which are isotropic on the sphere and vary only weakly with r.

The spatial dependence of $\langle \tilde{\delta}_i \tilde{\delta}^j \rangle$ means that the vector $\tilde{\delta}_i$ located at different points on $\mathbb{R}^3$ is not equally likely to be observed in a realization. Given $\langle \tilde{\delta}^2 \rangle$, $\langle \tilde{\delta}\tilde{\delta}_j \rangle$, and $\langle \tilde{\delta}_i \tilde{\delta}^j \rangle$, we can construct the ensemble average $\langle w_i^j \rangle$ in this coordinate system:

$$\langle w_i^{\,j} \rangle = \frac{1}{6} \int \Phi(X, x, y, z) \frac{\tilde{\delta}_i \tilde{\delta}^j}{|\nabla \tilde{\delta}|} \delta_D(\tilde{\delta} - \delta_t) dX, \qquad (50)$$
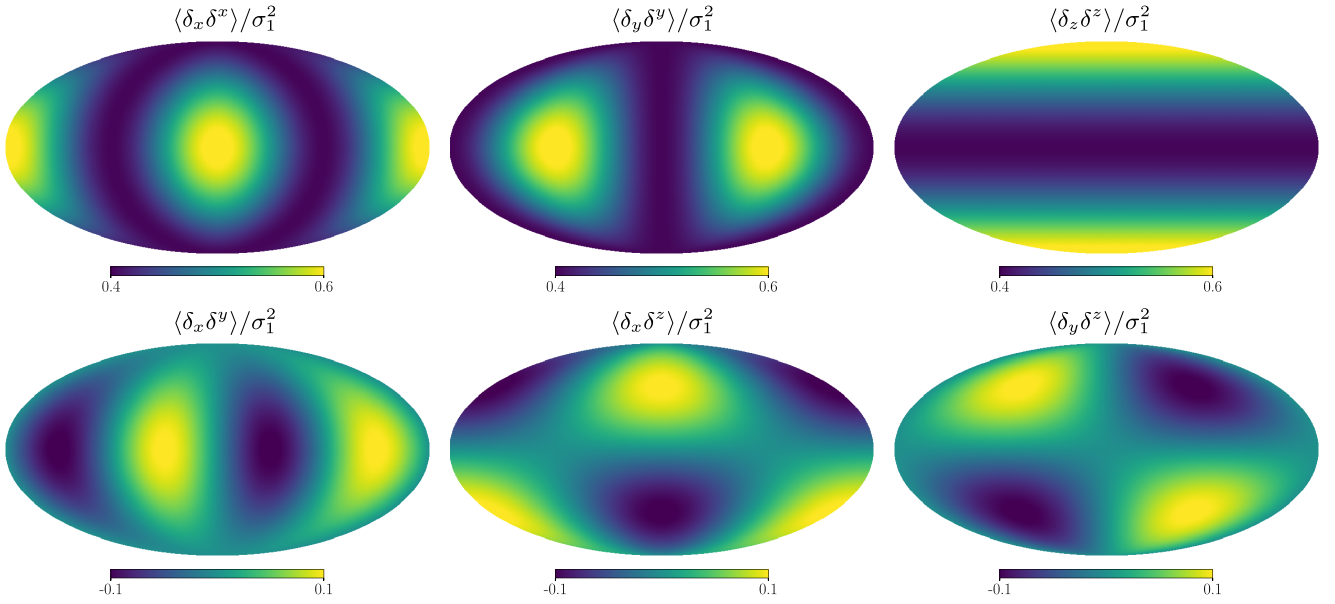
Figure 4. Cartesian cumulants $\langle \delta_i \delta^j \rangle / \sigma_1^2$ projected onto the two-sphere for fixed radial distance $r = 200$ Mpc from the central observer. The top row panels display the (x, x), (y, y), and (z, z) components from left to right, while the bottom row panels display the off-diagonal components (x, y), (x, z), and (y, z) components, from left to right.

where $\Sigma(x, y, z)$ is given by

$$\Sigma(x, y, z) = \begin{pmatrix} \langle \tilde{\delta}^2 \rangle & \langle \tilde{\delta}\tilde{\delta}_i \rangle \\ \langle \tilde{\delta}\tilde{\delta}^j \rangle & \langle \tilde{\delta}_i \tilde{\delta}^j \rangle \end{pmatrix}. \tag{51}$$

It is clear that the volume average $\bar{w}_i{}^j$ will not generically be representative of the ensemble average $\langle w_i^j \rangle$ in this coordinate system, due to the coordinate dependence of $\langle w_i^j \rangle$. For example, taking the all-sky spatial average of w_i^j extracted from a field with the particular cumulant pattern in Figure 4 will yield an isotropic result $\bar{w}_i{}^j \propto \delta_i{}^j$—we confirm this in the following section.[9] The volume average in this particular case would incorrectly identify the field as isotropic, because the spatial dependence of the signal in this coordinate system would be washed out by the averaging. If we take the volume average of the cumulant tensor $\langle \tilde{\delta}_i \tilde{\delta}^j \rangle$ over $\mathbb{S}^2$ and some arbitrary radial range, then the result will be proportional to the identity matrix. We can infer that the directional information is lost upon volume averaging. The volume and ensemble averages cannot be equated even approximately in this example. This conclusion is not in contradiction with the plane-parallel limit, because here we are considering an all-sky average. If we instead took a small patch on the sky and aligned the Cartesian coordinate system with one axis pointing to the patch, then the plane-parallel limit could be approximately realized.

The underlying point is that, for tensors and inhomogeneous fields, the volume average can reasonably approximate the ensemble average or completely misrepresent it, depending on the properties of the field and choice of coordinate system, volume, and transport path.

6. Numerical Extraction of Minkowski Tensors in Spherical Redshift Space

We now confirm numerically some of the results of the previous sections, and furthermore study the conditions under which we can faithfully extract the Kaiser signal from a redshift-space distorted, non-Gaussian matter field in the low redshift universe. The matter density field is assumed to be Gaussian in the early universe, but the nonlinear nature of gravitational collapse couples Fourier modes. This is a scale dependent statement, and by smoothing the late time density field over sufficiently large scales, the standard model of cosmology posits that the density field is perturbatively non-Gaussian. We attempt to extract the Kaiser RSD signal from the large-scale-averaged density field.

In this work, we do not pursue the computational challenges that come with real data, such as galaxy bias, shot noise, complex survey geometries, and Malmquist bias—these issues will be considered elsewhere. When galaxies are scattered radially, the relative volume difference along the line of sight can introduce a spurious radial gradient in the mean density, which must be carefully subtracted. Neglecting these subtleties, we focus specifically on two questions—can we use the volume average constructed in Section 4.2 as an unbiased estimate of the ensemble average derived in Section 4.1, and over what scales must we smooth the non-Gaussian dark matter field to reproduce the Gaussian limit of these statistics? We also compare the MTs extracted from plane-parallel and spherical redshift-space distorted fields and confirm that they are indistinguishable for fields occupying cosmological volumes.

To perform these tests, we use two data sets—initially Gaussian random fields and then dark matter particle distributions that have been gravitationally evolved to $z = 0$.

6.1. Gaussian Random Fields

For Gaussian random fields, we start by generating an isotropic and homogeneous field δ in a periodic cube of side length $L = 1490$ Mpc ($= 1000\,h^{-1}$Mpc), in Fourier space using

---

[9] Simply adding Cartesian components of w_i^j at different points of the manifold to obtain $\bar{w}_i{}^j$ implicitly assumes Euclidean path transport, but neglects the geodesic incompleteness of the manifold. Regardless, we do not use the Cartesian coordinate system other than to provide an example for which ergodicity fails.

an input linear ΛCDM matter power spectrum $P(k, R_G)$ at $z = 0$ with the cosmological parameters given in Table 1. We smooth the field with Gaussian kernel $W(kR_G) \propto e^{-k^2 R_G^2/2}$. The field is sampled on a Cartesian grid with $N_p = 512$ pixels per side, with resolution $\Delta = 2.9$ Mpc. We then create plane-parallel and spherical redshift-space distorted fields. For the plane-parallel case, we apply the standard operator (see Equation (8)) to δ, in Fourier space, using $f = \Omega_m^{6/11}$ and aligning the RSD correction with the e_z axis of the box.

To construct a spherically redshift-space distorted field, we generate a second isotropic field $\Omega \equiv \nabla^{-2}\delta$ on the grid, and construct the gradient $\nabla_i\Omega$ in the Cartesian coordinate system. Then we infer the radial derivative $\partial_r\Omega$ using a standard transformation (we provide our angle conventions explicitly in Equation (C15)). We repeat this procedure on $\partial_r\Omega$ on the lattice to obtain the second derivative $\partial_{rr}\Omega$, and finally define the spherically redshift-space distorted density field as

$$\tilde{\delta}_{\{m,n,p\}} = \delta_{\{m,n,p\}} + f\left(\partial_{rr}\Omega_{\{m,n,p\}} + \frac{2}{r}\partial_r\Omega_{\{m,n,p\}}\right). \quad (52)$$

This field is then masked such that $\tilde{\delta}_{\{m,n,p\}}$ is assigned zero value and not used in our analysis if the pixel $\{m, n, p\}$ is such that it is a radial distance from the *observer* at the center of the box, lies outside the range $100 < r \leqslant 630$ in Mpc units. We use *all-sky* data, taking the complete $4\pi r^2$ area on $\mathbb{S}^2$ relative to the central observer.

For each data set, we calculate the mean $\bar{\delta}$ and variance $\tilde{\sigma}_0^2$ of the unmasked pixels, and define the zero mean, unit variance field $(\tilde{\delta}_{\{m,n,p\}} - \bar{\delta})/\tilde{\sigma}_0$. The volume average $\bar{w}_i{}^j$ is calculated for each of the three data sets—isotropic, plane-parallel, and spherical redshift-space distorted. For the isotropic and plane-parallel fields, we use the entire box with periodic boundary conditions, and $\bar{w}_i{}^j$ is defined in the Cartesian coordinate system of the box. From the Cartesian lattice, we use a simple second-order accurate finite difference scheme to construct the gradients δ_i and $\tilde{\delta}_i$, and because we use Euclidean paths to collect tensors in $\mathbb{R}^3$, we can simply take a sum of $w_i{}^j_{\{m,n,p\}}$ pixels without any explicit transport transformation. Hence the volume averages are

$$^{\text{re}}\bar{w}_i{}^j = \frac{1}{6V}\sum_{m,n,p} \Delta^3\delta_D(\delta_{\{m,n,p\}} - \nu)\frac{\delta_{i\{m,n,p\}}\delta^j{}_{\{m,n,p\}}}{|\nabla\delta_{\{m,n,p\}}|}, \quad (53)$$

$$^{\text{pp}}\bar{w}_i{}^j = \frac{1}{6V}\sum_{m,n,p} \Delta^3\delta_D(\tilde{\delta}_{\{m,n,p\}} - \nu)\frac{\tilde{\delta}_{i\{m,n,p\}}\tilde{\delta}^j{}_{\{m,n,p\}}}{|\nabla\tilde{\delta}_{\{m,n,p\}}|}, \quad (54)$$

where the superscripts denote *real space* (re) and *plane parallel* (pp), and ν is the root mean square normalized threshold $\nu = \delta_t/\sigma_0$, or $\nu = \delta_t/\tilde{\sigma}_0$, respectively.

For the spherically distorted field, we follow the procedure outlined in Section 4.2; we randomly select an unmasked pixel $\{a, b, c\}$ as the fiducial point at which we take the spatial average, with the unit vector pointing to the pixel denoted $\hat{T}_2$. Then for each pixel selected by the discretized delta function $\delta_D(\tilde{\delta}_{\{m,n,p\}} - \nu) \neq 0$, we define the unit vector pointing to this pixel as $\hat{T}_1$, and use $\hat{T}_1$ and $\hat{T}_2$ to construct a unit quaternion q, which is used to rotate the Cartesian gradient vector, $\tilde{\delta}'_i = q\tilde{\delta}_i q^*$, reflecting its change of orientation when transported from $\hat{T}_1$ to $\hat{T}_2$. The components of the quaternion are given in Appendix C. At $\{a, b, c\}$, the rotated Cartesian gradient is transformed to the spherical coordinate basis e_r, e_θ,

e_ϕ. We present a schematic of this transport in Figure 3. Note that there is no unique rotation–great arc transport for pixels at antipodal points on the sphere to $\{a, b, c\}$; for these we select a random rotation axis in the plane perpendicular to $\hat{T}_2$ (we have confirmed that different choices do not affect our numerical results). The volume average for the spherically redshift-space distorted case (superscript $^{\text{sp}}$) is

$$^{\text{sp}}\bar{w}_i{}^j = \frac{1}{6V}\sum_{m,n,p} \Delta^3\delta_D(\tilde{\delta}_{\{m,n,p\}} - \nu)\frac{{}^\gamma\tilde{\delta}_{i\{m,n,p\}}{}^\gamma\tilde{\delta}^j{}_{\{m,n,p\}}}{|\nabla\tilde{\delta}_{\{m,n,p\}}|}, \quad (55)$$

where $^\gamma$ denotes great arc transport, and the tensor is defined in a spherical basis. We measure $\bar{w}_i{}^j$ over $N_\nu = 51$ threshold values ν equi-spaced over the range $-3.8 \leqslant \nu \leqslant 3.8$, for $N_{\text{real}} = 50$ realizations of a Gaussian random field. We repeat the measurements for fields smoothed with scale R_G over the range $15\,\text{Mpc} \leqslant R_G \leqslant 45\,\text{Mpc}$.

Before presenting the numerical results, we discuss a way to check the Gaussian nature of a random field. For a general weakly non-Gaussian field, we can expand the components of the MTs as a series of Hermite polynomials,[10] as follows:

$$\bar{w}_i{}^j = e^{-\nu^2/2}(A|_i^j H_0(\nu) + a_1|_i^j H_1(\nu) + a_2|_i^j H_2(\nu) + \ldots). \quad (56)$$

This expansion is equivalent to Matsubara's perturbative expansion for the scalar Minkowski functionals (Matsubara 2003), albeit the expansion coefficients are assigned to each Hermite polynomial and not to powers of the variance. The coefficients contain information of the generalized skewness, kurtosis, and higher moments of the field. The coefficients $A|_i^j$, $a_1|_i^j$, $a_2|_i^j$ can be computed using the orthogonality properties of the Hermite polynomials, as

$$A|_i{}^j = \frac{1}{\sqrt{2\pi}}\int_{-\nu_{\text{max}}}^{\nu_{\text{max}}} \bar{w}_i{}^j(\nu)H_0(\nu)d\nu, \quad (57)$$

$$a_1|_i{}^j = \frac{1}{\sqrt{2\pi}}\int_{-\nu_{\text{max}}}^{\nu_{\text{max}}} \bar{w}_i{}^j(\nu)H_1(\nu)d\nu, \quad (58)$$

$$a_2|_i{}^j = \frac{1}{2\sqrt{2\pi}}\int_{-\nu_{\text{max}}}^{\nu_{\text{max}}} \bar{w}_i{}^j(\nu)H_2(\nu)d\nu, \quad (59)$$

where $\nu_{\text{max}} \to \infty$. For our analysis, we take $\nu_{\text{max}} = 3.8$, after checking that our results are not sensitive to reasonable variations of this value.[11] For Gaussian random fields, the coefficients of the higher-order terms in the expansion a_1, a_2 etc. should be consistent with 0 in real and redshift space, so we refer to the coefficient of $H_0(\nu)$ as the *amplitude* of the MT components.

Using the above way of representing weakly non-Gaussian random fields, in the Gaussian and plane-parallel limits, we have (Appleby et al. 2019)

$$^{\text{pp}}\bar{w}_i{}^j = {}^{\text{pp}}A_G|_i{}^j H_0(\nu)e^{-\nu^2/2} \quad (60)$$

---

[10] $H_n(\nu)$ are the probabilist's Hermite polynomials, the first few of which are given by $H_0(\nu) = 1$, $H_1(\nu) = \nu$, $H_2(\nu) = \nu^2 - 1$.
[11] The Hermite polynomials are exactly orthogonal only in the limit $\nu_{\text{max}} \to \infty$. However, since $\bar{w}_i{}^j$ is exponentially damped at large thresholds, it suffices to choose finite ν_{max}. Taking ν_{max} to be too large in a finite volume data set can generate biased values of the Hermite polynomial coefficients (see Appendix A-4 of Appleby et al. 2021).

with

$$^{\mathrm{pp}}A_G|_x{}^x = \frac{A_0}{4}\left[\frac{(2\lambda^2 - 1)\cosh^{-1}(2\lambda^2 - 1)}{(\lambda^2 - 1)^{3/2}} - \frac{2\lambda}{\lambda^2 - 1}\right],$$
(61)

$$^{\mathrm{pp}}A_G|_y{}^y = {}^{\mathrm{pp}}A_G|_x{}^x,$$
(62)

$$^{\mathrm{pp}}A_G|_z{}^z = A_0\left(\frac{\lambda^2}{\lambda^2 - 1}\right)\left(\lambda - \frac{\cosh^{-1}\lambda}{\sqrt{\lambda^2 - 1}}\right),$$
(63)

where A_0 and λ are defined in Equations (18) and (19). In real space, we have (Appleby et al. 2018b)

$$^{\mathrm{re}}A_G|_x{}^x = {}^{\mathrm{re}}A_G|_y{}^y = {}^{\mathrm{re}}A_G|_z{}^z = \frac{\sigma_1}{9\sqrt{3}\,\pi\sigma_0}.$$
(64)

For the Minkowski functional W_1, the coefficient a_1 of $H_1(\nu)$ is one of two terms induced as a leading-order non-Gaussian correction, and a_2 is one of several higher-order contributions. Hence we use these terms as proxies to study the non-Gaussian corrections of the MTs that are induced by gravitational collapse. As mentioned above, for the Gaussian random fields considered in this subsection, a_1 and a_2 should be consistent with 0 in real, plane-parallel, and spherical redshift space. The RSD operator does not change the Gaussian nature of the field. We check that the numerically computed values of a_1 and a_2 are consistent with 0 in our calculations, when measuring the MT of Gaussian random fields.

In Figure 5 (top left panel), we present the diagonal and off-diagonal components of $^{\mathrm{re}}\bar{w}_i{}^j$ and $^{\mathrm{sp}}\bar{w}_i{}^j$ extracted from the fields smoothed with $R_G = 20$ Mpc. The points and error bars correspond to the mean and root mean square of the realizations; hence we are presenting the ensemble average of the volume average. The filled and open diamonds are measurements in spherical redshift and real space respectively. The diagonal components in real space are equal, modulo of a noise component (see light green and/or blue and/or red open diamonds). The real-space volume average satisfies $^{\mathrm{re}}\bar{w}_i{}^j \propto \delta_i{}^j$ in every coordinate system. In redshift space, the radial component of $\bar{w}_i{}^j$ is significantly larger than the angular components—this is the Kaiser signal. The off-diagonal components of $^{\mathrm{re}}\bar{w}_i{}^j$, $^{\mathrm{pp}}\bar{w}_i{}^j$, and $^{\mathrm{sp}}\bar{w}_i{}^j$ are all consistent with 0. The error bars are the statistical uncertainty of the measurements, which increase for increasing R_G because we are using a simulation box of fixed size.

In Figure 5, we present the values of $A|_i^{j}$ (top right panel), $a_1|_i^{j}$ (bottom left panel), and $a_2|_i^{j}$ (bottom right panel) for $\bar{w}_i{}^j$ extracted from the real and spherical redshift-space distorted fields as a function of smoothing scale R_G. In the top right panel, the solid and/or dashed gold lines are the corresponding plane-parallel Kaiser limits given in Equations (61)–(63), and the solid silver line is the isotropic expectation value in Equation (64).

The volume averages $^{\mathrm{re}}\bar{w}_i{}^j$ and $^{\mathrm{sp}}\bar{w}_i{}^j$ extracted from the spherical RSD and real-space data sets match the ensemble averages derived in Appleby et al. (2018b, 2019). Similarly the coefficients a_1, a_2 are consistent with 0 at all scales probed (see bottom panels). This is expected—we generated Gaussian random fields, and the application of the linear RSD operator preserves Gaussianity. This provides a check on the ergodicity condition $\langle w_i{}^j\rangle \simeq \bar{w}_i{}^j$, and indicates that our definition of the volume average can be used to reproduce the ensemble average.

Finally, in Figure 6, we present the fractional differences $(^{\mathrm{sp}}A|_i^{j} - {}^{\mathrm{pp}}A|_i^{j})/{}^{\mathrm{pp}}A|_i^{j}$ (left panel), $(^{\mathrm{sp}}a_1|_i^{j} - {}^{\mathrm{pp}}a_1|_i^{j})/{}^{\mathrm{pp}}A_G|_i^{j}$ (central panel), and $(^{\mathrm{sp}}a_2|_i^{j} - {}^{\mathrm{pp}}a_2|_i^{j})/{}^{\mathrm{pp}}A_G|_i^{j}$ (right panel) as a function of smoothing scale R_G. These quantities are all consistent with 0 at all scales probed, confirming that the plane-parallel and spherical redshift-space distorted fields are statistically indistinguishable for data that are at cosmological distance >100 Mpc from the observer.

6.2. Non-Gaussian Dark Matter Fields

To study the gravitationally evolved non-Gaussian dark matter density field, we use $N_{\mathrm{real}} = 50$, $z = 0$ snapshot boxes from the Quijote simulations (Villaescusa-Navarro et al. 2020). These are a suite of cosmological scale dark matter simulations in which $\sim 44{,}000$ realizations of 512^3 particles are gravitationally evolved in boxes of size $L = 1490$ Mpc ($= 1000\,h^{-1}$Mpc), from $z = 127$ to $z = 0$. We take $N_{\mathrm{real}} = 50$, $z = 0$ snapshot boxes and generate real-space density fields by binning the dark matter particles into a regular 512^3 Cartesian grid of resolution $\Delta = 2.9$ Mpc using a cloud-in-cell scheme. Defining the number density field $\delta_{\{i,j,k\}} = (n_{\{i,j,k\}} - \bar{n})/\bar{n}$, where $n_{\{i,j,k\}}$ is the number of particles in the $\{i, j, k\}$ pixel, and $\bar{n}$ is the mean number of particles per pixel. We smooth this field with a Gaussian kernel $W(kR_G) \propto e^{-k^2R_G^2/2}$ in Fourier space. In this work, we exclusively work with dark matter data because we focus on the question of the scale at which the Gaussian, Kaiser limit of the density field is reached. Using galaxy data introduces additional complications, as the choice of galaxy sampling will affect small scale velocity dispersion, which will impact the radial component of the statistics. The galaxy density field—both mock and actual data—will be studied in the future.

To generate the plane-parallel and spherical redshift-space distorted fields, we take the real-space positions of the particles $\boldsymbol{x}$ and perturb them according to

$$\boldsymbol{s} = \boldsymbol{x} + \boldsymbol{e}_z(\boldsymbol{v}.\boldsymbol{e}_z)\frac{(1 + z)}{H(z)},$$
(65)

$$\boldsymbol{s} = \boldsymbol{x} + \boldsymbol{e}_r(\boldsymbol{v}.\boldsymbol{e}_r)\frac{(1 + z)}{H(z)},$$
(66)

respectively, where $\boldsymbol{v}$ is the velocity of the particle, $\boldsymbol{e}_z$ is the unit vector aligned with the z-direction of the Cartesian grid, and $\boldsymbol{e}_r$ is the radial basis vector to the particle from an observer at the center of the box. We take redshift zero snapshot boxes, so we fix $z = 0$, and $H(z) = H_0$.

For the redshift-space distorted fields, we bin the particles into pixels with the cloud-in-cell scheme according to their redshift-space position, using the same $\Delta = 2.90$ Mpc Cartesian grid. We apply periodic boundary conditions for the plane-parallel corrected box along $\boldsymbol{e}_z$, which renders the field homogeneous but anisotropic. The spherical RSD operator is incompatible with periodicity. So we exclude all pixels that lie at distances $r \leqslant 50$ Mpc, and $r \geqslant 700$ Mpc from the central observer in our calculations of $\bar{w}_i{}^j$. The outer boundary of the shell is at least 50 Mpc from the edges of the box, so all particles affected by the periodic boundary are excluded. Finally, we smooth these pixel boxes with Gaussian kernel $W(kR_G) \propto e^{-k^2R_G^2/2}$ in Fourier space, and then further exclude all pixels that lie a distance $r \leqslant 100$ Mpc, and $r \geqslant 670$ Mpc
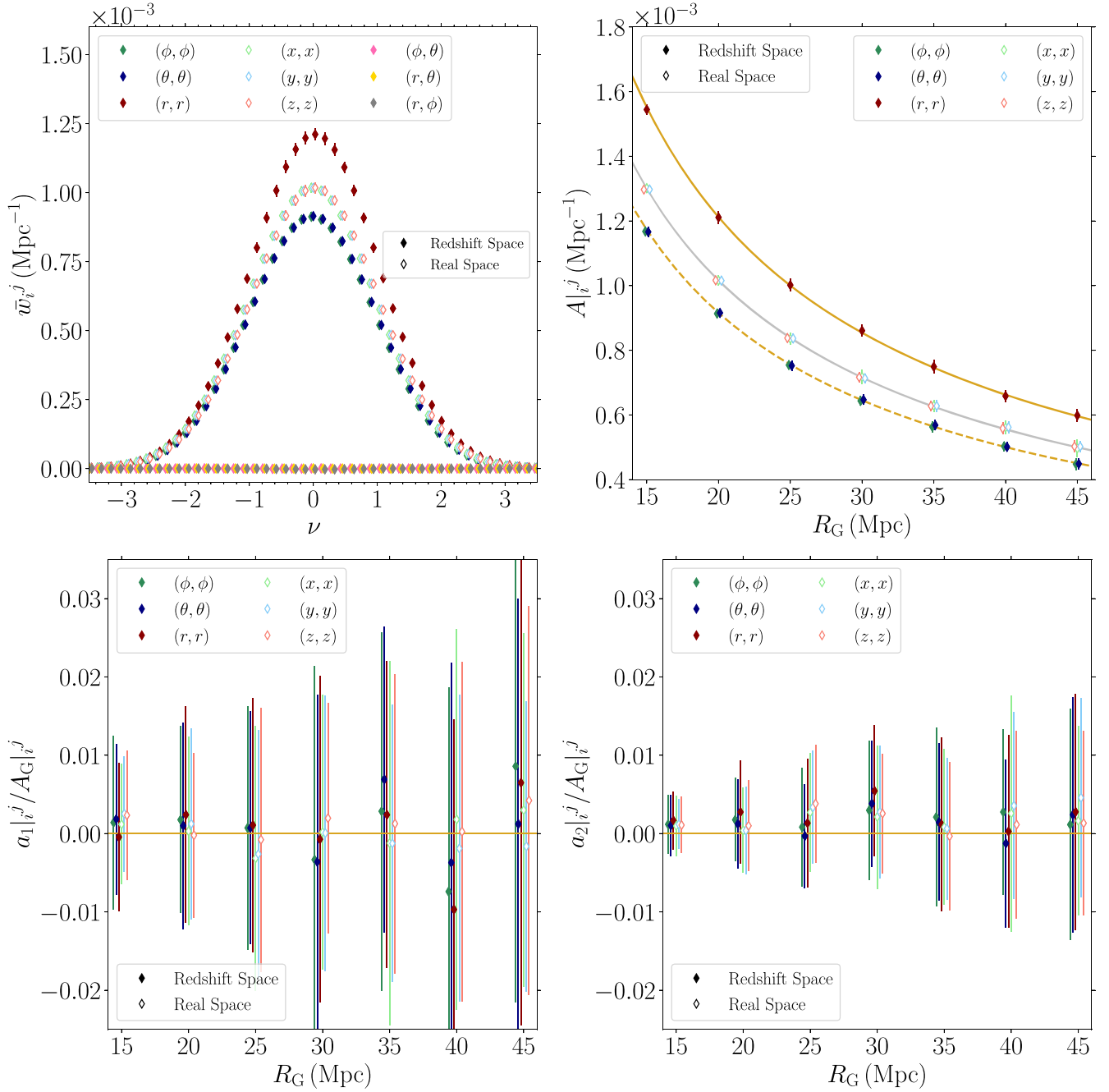
Figure 5. Top left panel: components of the Minkowski tensor extracted from a Gaussian random field in real space (open diamonds), and spherical redshift space (filled diamonds). The off-diagonal elements for the spherical redshift-space field are also presented and consistent with 0. The field has been smoothed with scale $R_G = 20$ Mpc. Top right panel: the amplitude of $\bar{w}_i{}^j$ as a function of smoothing scale of the field. The solid and/or dashed gold lines are the plane-parallel expectation values in redshift space, and the solid silver line is the isotropic expectation value. Bottom panels: the coefficients of the $H_1(\nu)$ (left), $H_2(\nu)$ (right) Hermite polynomials. They are consistent with 0 for a Gaussian field, in both real and redshift space.

from the central observer. This last step eliminates pixels that are affected by sampling near the boundary. The end result is a set of three fields from which we extract ${}^{re}\bar{w}_i{}^j$, ${}^{pp}\bar{w}_i{}^j$, and ${}^{sp}\bar{w}_i{}^j$.

We calculate the mean $\bar{\delta}$ and variance $\tilde{\sigma}_0^2$ of the unmasked pixels for each field, and define the zero mean, unit variance quantity $(\tilde{\delta}_{\{m,n,p\}} - \bar{\delta})/\tilde{\sigma}_0$. The quantities ${}^{re}\bar{w}_i{}^j$, ${}^{pp}\bar{w}_i{}^j$, and ${}^{sp}\bar{w}_i{}^j$ are measured over $n_\nu = 301$ values of threshold density ν from the minimum and maximum values of the field in each simulation. We then rescale the isodensity threshold ν to ν_A, where ν_A is the threshold for which the excursion set has the

same volume fraction as a corresponding Gaussian field:

$$f_A = \frac{1}{\sqrt{2\pi}} \int_{\nu_A}^{\infty} e^{-t^2/2} \, dt, \qquad (67)$$

where f_A is the fractional volume of the field above ν_A. Expressing the MTs as a function of ν_A as opposed to ν partially Gaussianizes the statistics (Gott et al. 1987; Weinberg et al. 1987; Melott et al. 1988). To perform this rescaling, we use spline interpolation on the $W_1^{0,2}$ versus ν calculated data
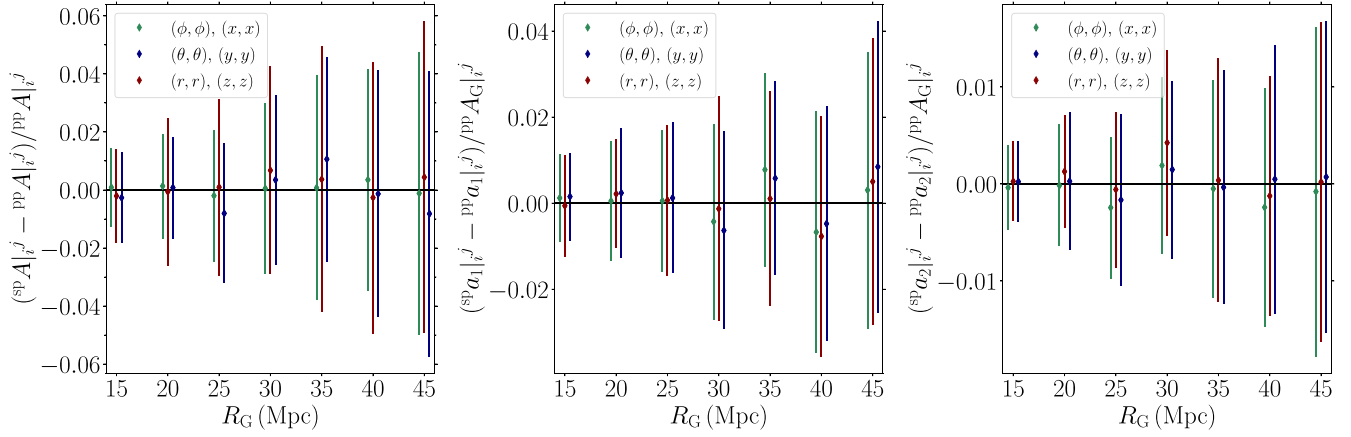
Figure 6. Fractional difference between $A|_i^j$ (left), $a_1|_i^j$ (middle), and $a_2|_i^j$ (right) extracted from the spherical and plane-parallel redshift-space distorted Gaussian random fields.

and construct $W_1^{0,2}$ versus ν_A, at $n_{\nu_A} = 41$ values, equi-spaced over the range $-3.8 < \nu_A < 3.8$.

In Figure 7, we present the components of the MT ${}^{\rm sp}\bar{w}_i{}^j$ as a function of ν (top left panel) and ν_A (top middle panel) for the fields smoothed with comoving scale $R_{\rm G} = 20$ Mpc. The off-diagonal components are presented in the top right panel and are consistent with 0. The same is true for all smoothing scales tested in this work. The top panels represent the components of ${}^{\rm sp}\bar{w}_i{}^j$ in the spherical basis. In the bottom panels of Figure 7, we present the components of ${}^{\rm sp}\bar{w}_i{}^j$ in a Cartesian basis, calculated using Euclidean paths to transport tensors to a common location on the manifold. We plot the (x, x), (y, y), (z, z) components as a function of ν (left), ν_A (middle), and the off-diagonal elements (right panel). The MTs in the top and bottom panels are both extracted from the same spherical redshift-space distorted density field; only the coordinate systems and choice of transport paths differ. In the bottom panels, we observe that the diagonal elements of the MT are statistically equivalent, and the off-diagonal elements are consistent with zero. Hence ${}^{\rm sp}\bar{w}_i{}^j \propto \delta_i{}^j$, and the volume average incorrectly infers that the field is isotropic. As discussed in Section 5, in a Cartesian basis, the spherical RSD operator generates spatially dependent cumulants, and taking the volume average washes out the anisotropic signal.

Next we explore the information contained in the coefficients A, a_1, and a_2 defined in Section 6.1. In the top left panel of Figure 8, we present the components $A|_i^j$ with $(i, j) = (r, r)$, (θ, θ), (ϕ, ϕ) (dark red, blue, green filled diamonds respectively) in redshift space. The points and error bars are the mean and rms values of the $N = 50$ snapshot boxes, and the points that overlap have been slightly perturbed for visual clarity. For comparison we also show the expectation values for ${}^{\rm sp}A_G|_r^r$ (solid gold line), and ${}^{\rm sp}A_G|_\theta^\theta = {}^{\rm sp}A_G|_\phi^\phi$ (dashed gold line), in the limit $r \to \infty$ for a Gaussian random field with a linear ΛCDM power spectrum and the same cosmological parameters as the Quijote simulations. In the top right panel, we exhibit the ratio of ${}^{\rm sp}A|_i^j$ extracted from the Quijote simulations and the Gaussian plane-parallel expectation values from Equations (61)–(63). We also present ${}^{\rm re}A|_i{}^j$ divided by the isotropic expectation value from Equation (64), with $(i, j) = (x, x)$, (y, y), (z, z) (light red, blue, green open diamonds respectively) extracted from the corresponding real-space snapshot boxes without any velocity correction applied to the particle positions.

The results for the isotropic field (light open diamonds) present no surprises. The amplitude of each component (x, x), (y, y), (z, z) are statistically indistinguishable, and the Gaussian limit is an excellent approximation at quasi-linear scales $R_G \gtrsim 30$ Mpc (see top panels). Below this scale, the amplitude of the MT components starts to drop relative to the Gaussian expectation (see top right panel). This is due to the "gravitational smoothing" effect first observed in Melott et al. (1988) for the scalar functionals. The a_1 component (see bottom left) is consistent with 0 on large scales, but is $\mathcal{O}(0.01)$ at quasi-linear scales $R_G \sim 25$ Mpc. The a_2 term (see bottom right), which we expect to be induced at higher order in a σ_0 expansion of non-Gaussianity, is consistent with 0 at all scales probed.

In redshift space (dark filled diamonds), the picture changes considerably. The most striking difference is the strong departure of ${}^{\rm sp}A|_r^r$ from its Gaussian expectation value (see red filled diamonds, top panels). Even on large scales $R_G \sim 40$ Mpc, the Gaussian, Kaiser formula of Equation (61) is not a particularly good approximation. In contrast, the Kaiser approximation of Equations (62), (63) is excellent for the perpendicular components (green and/or blue filled diamonds, top panels). It was noted in Kim et al. (2014) that the Gaussian, Kaiser limit is only a good approximation for the scalar Minkowski functionals when the density field is smoothed on very large scales. Our results support this statement, and further show that the radial component of the field is the origin of the breakdown. In addition to the decrease in $A|_r^r$, the non-Gaussian terms $a_{1,2}|_i^j$ are larger for the (r, r) component in redshift space, but remain small at the scales probed. The fact that a_2 is induced at a statistically significant level on scales $R_G \leqslant 20$ Mpc suggests that novel non-Gaussian contributions are induced in redshift space (see red filled diamonds, lower right panel).

In Appleby et al. (2019), it was noted that the ratio of parallel and perpendicular components of the MT would provide a relatively pure measurement of f (or $\beta = f/b$ for biased tracers). However, it is clear that ${}^{\rm sp}A|_r^r$ strays far from the Kaiser limit. The perpendicular components ${}^{\rm sp}A|_\theta^\theta$, ${}^{\rm sp}A|_\phi^\phi$ remain closer to their Gaussian expectation values on small scales, but their values are not sensitive to f alone. Specifically, each individual component of the MTs is sensitive to n_s, $\Omega_c h^2$, and f. Measuring the ratios ${}^{\rm sp}A|_\theta^\theta/{}^{\rm sp}A|_r^r$, ${}^{\rm sp}A|_\phi^\phi/{}^{\rm sp}A|_r^r$ would potentially break these

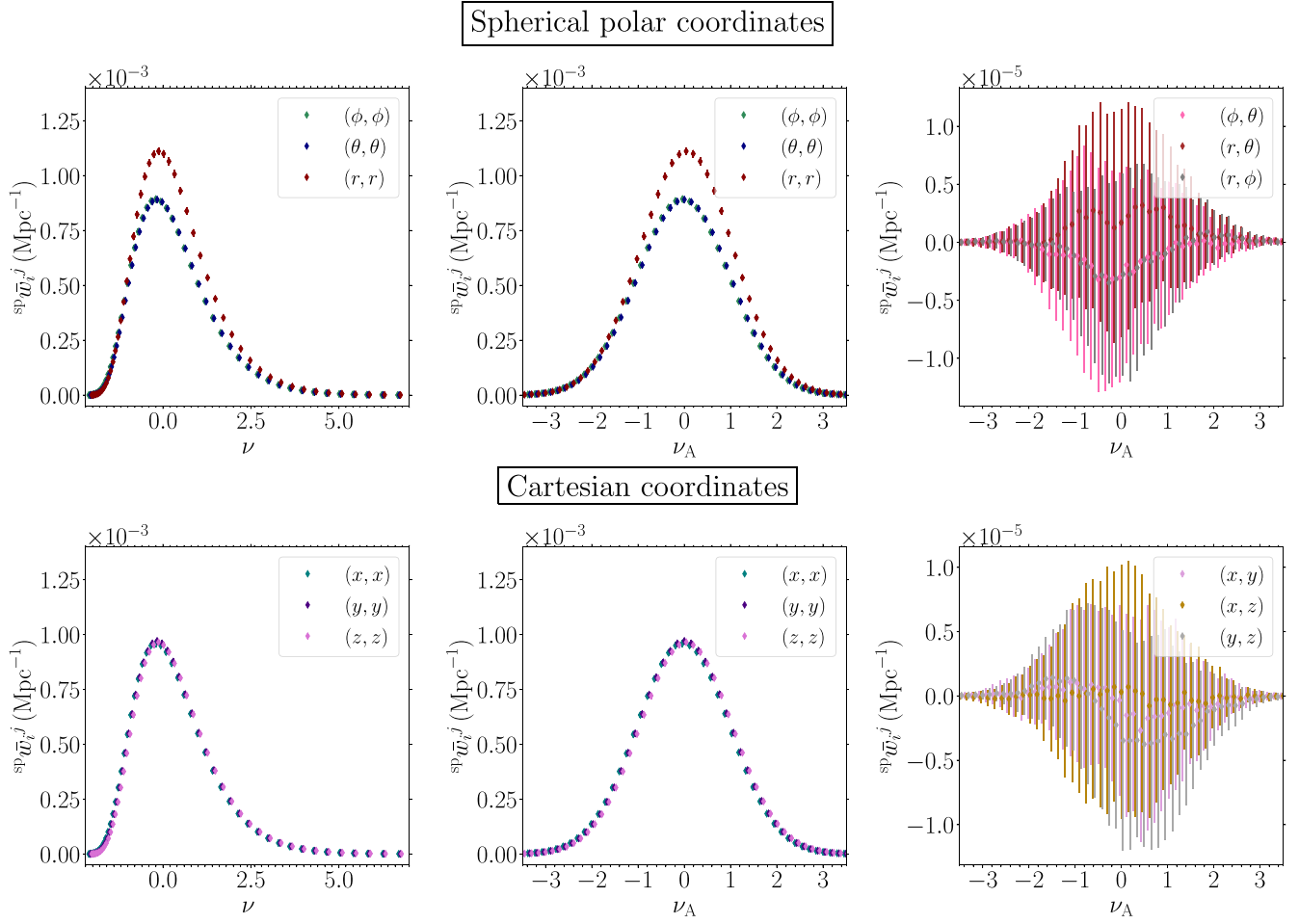## Spherical polar coordinates

Cartesian coordinates

Figure 7. The Minkowski Tensors measured from $N_{\rm real} = 50$ redshift-space distorted Quijote dark matter simulations, as a function of the thresholds ν, and the rescaled thresholds ν_A. The top panels display $^{\rm sp}\bar{w}_i{}^j$ from the spherically redshift-space distorted fields in a spherical coordinate system, while the bottom panels show $\bar{w}_i{}^j$ extracted from the same spherical RSD fields but in a Cartesian coordinate system.

degeneracies, but only after we have resolved the origin of the $^{\rm sp}A|_r^r$ behavior.

The large departure of $^{\rm sp}A|_r^r$ from the Kaiser limit is not due to the imposition of the spherical RSD operator. To highlight this, in Figure 9, we present the fractional differences $(^{\rm sp}A|_i^j - {}^{\rm pp}A|_i^j)/^{\rm pp}A|_i^j$ (left panel), $(^{\rm sp}a_1|_i^j - {}^{\rm pp}a_1|_i^j)/^{\rm pp}A_{\rm G}|_i^j$ (central panel), and $(^{\rm sp}a_2|_i^j - {}^{\rm pp}a_2|_i^j)/^{\rm pp}A_{\rm G}|_i^j$ (right panel). All three fractional differences are consistent with 0 over all scales probed in this work, meaning that the spherical and plane-parallel redshift-space fields possess statistically indistinguishable MT functionals, similar to the Gaussian random fields in the previous subsection.

6.3. Non-Gaussian Effects along the Line of Sight

The significant drop in the amplitude of the MT component parallel to the line of sight on small scales observed in the previous subsection can be interpreted as the Finger of God effect, which scatters particle positions over megaparsec scales due to the large peculiar velocity dispersion $\sigma_{\rm pec}$ associated with bound structures (Jackson 1972). The dominant effect of $\sigma_{\rm pec}$ is an amplitude decrease in $A|_r^r$, which is consistent with an additional, anisotropic damping factor acting on the power spectrum. The Finger of God effect has a long history within theoretical and observational cosmology (Jackson 1972;

Park et al. 1994; Fisher 1995), and it is well known that its effect on the power spectrum is imprinted even on relatively large scales (Juszkiewicz et al. 1998; Hikage & Yamamoto 2013; Beutler et al. 2014; Reid et al. 2014; Okumura et al. 2015; Tonegawa et al. 2020). Observations of the two-point functions indicate that the Kaiser limit is only accurate on the largest scales (Scoccimarro 2004; Jennings et al. 2011, 2010; Okumura & Jing 2010; Kwan et al. 2012; White et al. 2014).

Our analysis provides two new insights into this phenomenon in the context of the Minkowski statistics. First, the components of the MT perpendicular to the line of sight remain well described by the Kaiser approximation, even on relatively small scales $R_{\rm G} \gtrsim 25\,{\rm Mpc}$. Second, on *small scales* $R_{\rm G} \lesssim 20\,{\rm Mpc}$, the non-Gaussianity of the components $\bar{w}_r{}^r$ and $\bar{w}_\theta{}^\theta$ differ with considerable statistical significance; this can be observed in the $a_2|_i^j$ coefficient in Figure 8 (bottom right panel). This indicates that the additional non-Gaussian effects are induced in redshift-space parallel to the line of sight.

Regarding the amplitude decrease in the $A|_r^r$ component, we can attempt to model this effect using the standard approach in the literature—following Peebles (1976), Peacock & Dodds (1994), Park et al. (1994), Desjacques & Sheth (2010), Scoccimarro (2004), we introduce an additional damping kernel $P(k, R_{\rm G}) \rightarrow P(k, R_{\rm G})e^{-k_\parallel^2 \sigma_{\rm pec}^2}$ into the power spectrum
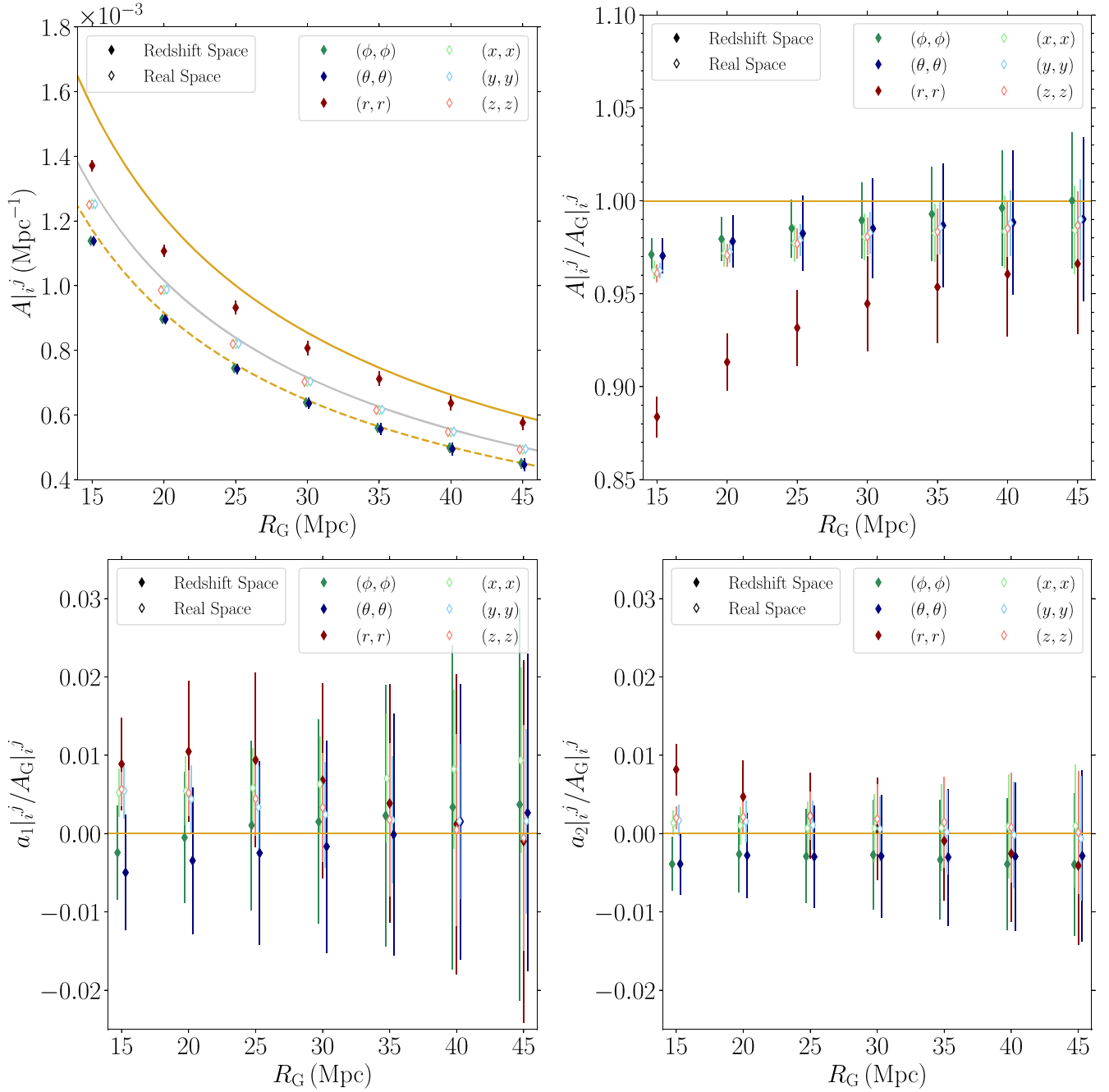
Figure 8. $A|_i^j$ (top left), $a_1|_i^j$ (lower left), and $a_2|_i^j$ (lower right) quantities as defined in Equations (57), (58), and (59) measured from $N_{\rm real} = 50$ Quijote simulations, at $z = 0$, in real and redshift space. The solid and/or dashed gold lines in the top left panel represent the expectation values of the radial/angular components for a Gaussian field in the plane-parallel limit, and the silver line is the isotropic Gaussian expectation value. The top right panel shows the fractional difference between the Quijote measurements of $A|_i^j$ and the Gaussian limit of this quantity in real and redshift space.

that is used in defining the cumulants. Returning to the plane-parallel limit, we can write the cumulants in redshift space as

$$\tilde{\sigma}_0^2 \equiv \langle \tilde{\delta}(\boldsymbol{x}')\tilde{\delta}(\boldsymbol{x}) \rangle|_{\boldsymbol{x}' \to \boldsymbol{x}} = \frac{1}{(2\pi)^2} \int_{-1}^{1} d\mu \int_0^\infty$$
$$\times \, dk k^2 (1 + f\mu^2)^2 P(k, R_{\rm G}) e^{-k^2 R_{\rm G}^2} e^{-k^2 \mu^2 \sigma_{\rm pec}^2}, \qquad (68)$$

$$\tilde{\sigma}_z^2 \equiv \langle \tilde{\delta}_z(\boldsymbol{x}')\tilde{\delta}_z(\boldsymbol{x}) \rangle|_{\boldsymbol{x}' \to \boldsymbol{x}} = \frac{1}{(2\pi)^2} \int_{-1}^{1} d\mu \int_0^\infty$$
$$\times \, dk k^4 \mu^2 (1 + f\mu^2)^2 P(k, R_{\rm G}) e^{-k^2 R_{\rm G}^2} e^{-k^2 \mu^2 \sigma_{\rm pec}^2}, \qquad (69)$$

$$\tilde{\sigma}_x^2 \equiv \langle \tilde{\delta}_x(\boldsymbol{x}')\tilde{\delta}_x(\boldsymbol{x}) \rangle|_{\boldsymbol{x}' \to \boldsymbol{x}} = \frac{1}{2(2\pi)^2} \int_{-1}^{1} d\mu \int_0^\infty$$
$$\times \, dk k^4 (1 - \mu^2)(1 + f\mu^2)^2 P(k, R_{\rm G}) e^{-k^2 R_{\rm G}^2} e^{-k^2 \mu^2 \sigma_{\rm pec}^2}, \quad (70)$$

$$\tilde{\sigma}_y^2 = \tilde{\sigma}_x^2, \qquad (71)$$

where $\sigma_{\rm pec}$ is a free parameter that describes the velocity dispersion of tracer particles within bound structures, and $\mu^2 \equiv k_z^2/k^2$. If we use these cumulants to derive the ensemble average $\langle^{\rm pp}\bar{w}_i{}^j \rangle$, the additional anisotropic exponential damping term due to the Finger of God effect introduces a significant
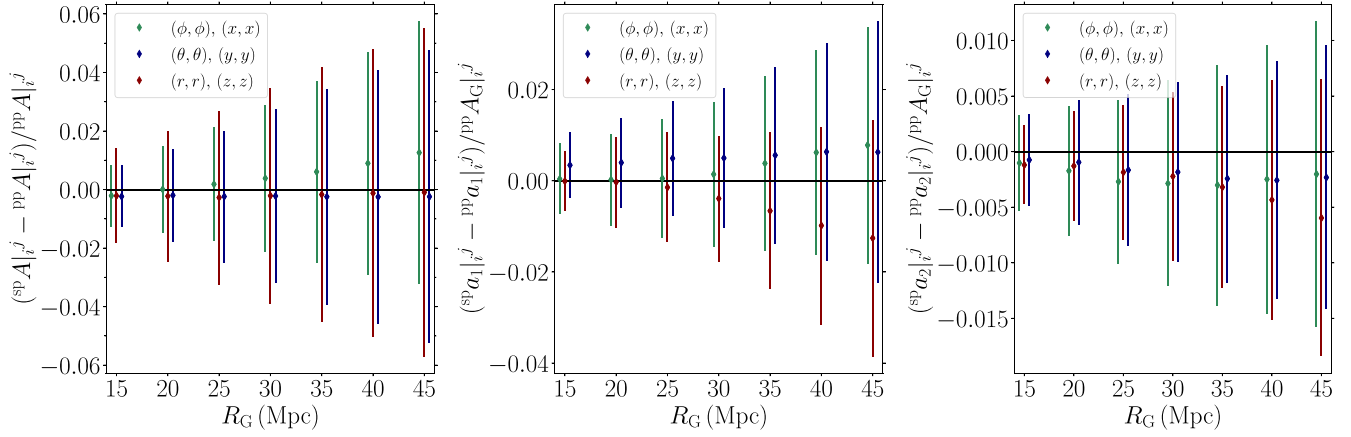
Figure 9. Fractional difference between $A|_i^j$ (left), $a_1|_i^j$ (middle), and $a_2|_i^j$ (right) extracted from the spherical and plane-parallel redshift-space distorted Quijote dark matter snapshot boxes.
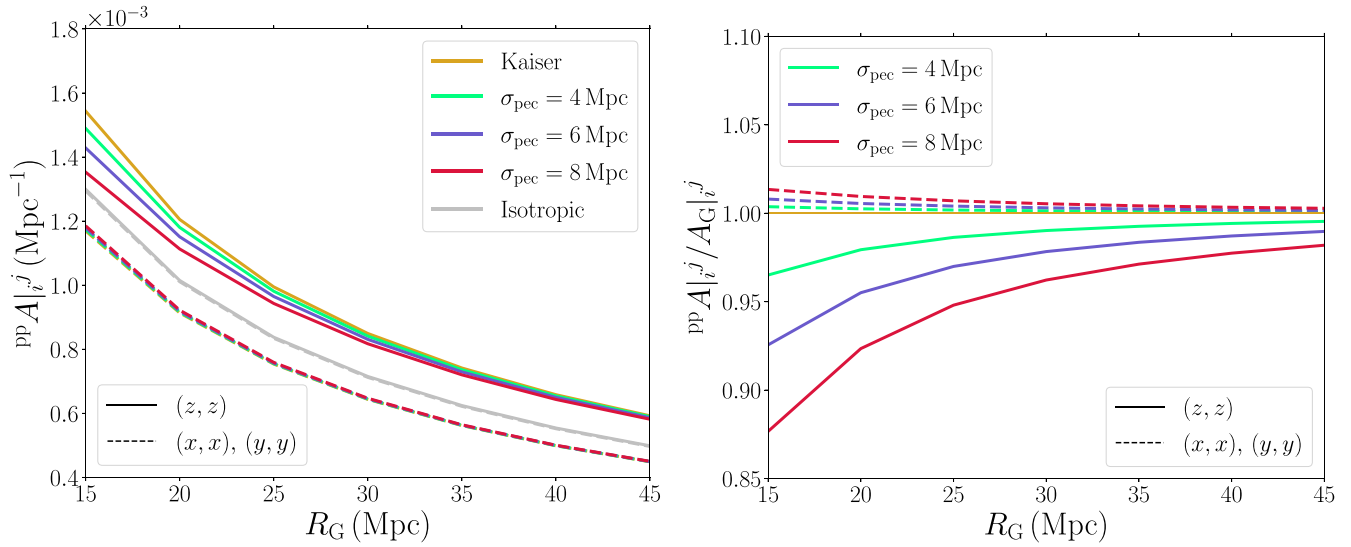

Figure 10. The effect of an exponential Finger of God damping term on the amplitude of the Minkowski tensor components in plane-parallel redshift space as a function of smoothing scale R_G.

drop in the (z, z) component, but does not have a large effect on the perpendicular (x, x), (y, y) elements. The amplitudes $^{pp}A_i^j$ as a function of R_G are presented in the left panel of Figure 10, keeping all parameters fixed and varying $\sigma_{pec} = 0, 4, 6, 8$ Mpc (yellow, green, blue, red lines respectively). The components parallel and perpendicular to the line of sight are presented as solid and/or dashed lines respectively, and we have included the isotropic limit $f = \sigma_{pec} = 0$ (silver lines), and Kaiser limit $\sigma_{pec} = 0$ (yellow lines). The right panel exhibits the ratio of the Finger of God affected ensemble averages to the Kaiser limit. The large decrease in the parallel cumulant is clearly observed on all scales, and the result is in qualitative agreement with the dark matter snapshot results (see top right panel of Figure 8). The perpendicular components increase by ~1%–2% relative to the Kaiser approximation. We also observe this effect in the dark matter data—in the top right panel of Figure 8, the (θ, θ), (ϕ, ϕ) components in redshift space are marginally higher than the isotropic components (top right panel, blue and/or green filled diamonds and light blue and/or green and/or red open diamonds respectively). However, in the dark matter snapshot

case, all components in real and redshift spaces have a systematically lower amplitude relative to the Gaussian limit due to the non-Gaussianity of the field (see top right panel, Figure 8), which requires further modeling.

Attempting to simultaneously constrain n_s, $\Omega_c h^2$, f, and σ_{pec} from the MTs will yield strong degeneracies. Potentially some of these can be broken because the Finger of God contribution is scale dependent (see Figure 10), while the Kaiser signal is independent of our choice of R_G. Hence measuring the MTs at multiple scales will provide simultaneous constraints on σ_{pec} and f. We must be careful to check for additional, non-Gaussian effects because these will also be scale dependent. A study of perturbative non-Gaussianity in redshift space is beyond the scope of this work and will be conducted elsewhere.

An alternative approach to mitigating the Finger of God effect is to iteratively correct galaxy positions using some higher-order prescription (Nusser et al. 1991; Gramann 1993; Narayanan & Weinberg 1998; Park et al. 2010), to reduce the large scatter induced by stochastic velocities within bound structures. This method attempts to reconstruct the galaxy density field in redshift space, but with nonlinear effects

removed. Many such reconstruction methods rely on the plane-parallel approximation, so this approach requires further development to be applied to radial RSD. A comparison of these different approaches will be a direction of future study.

7. Discussion

We have presented an analysis of the rank (2) tensor Minkowski functionals for an anisotropic and inhomogeneous Gaussian random field, in particular an isotropic and homogeneous field that has been subjected to the spherically symmetric RSD operator. Anisotropy here means that the structures in the field share a common alignment along the radial direction, leading to an inequality in the diagonal components of the MTs parallel and perpendicular to the line of sight. The inhomogeneity of the field introduces some significant pitfalls—the ensemble average is now a function of position on the manifold, and the volume average of the statistics will not necessarily be representative of the ensemble average. This statement depends on the coordinate system selected, the volume occupied by the field, and also the choice of path transport used to define a volume average of the tensors.

For the spherically redshift-space distorted field, there is a singularity in the cumulants at $r = 0$, which indicates that this point must be excised from the manifold. This fact, in conjunction with the assumed symmetry properties of the field—isotropic on $\mathbb{S}^2$—suggests that spherical coordinates and great arc transport provide a natural framework to measure the MTs. We constructed the cumulants of the density field and the gradient in this system and found that they are only weakly coordinate dependent at large distances from a central observer at $r = 0$, and furthermore are insensitive to angular position on $\mathbb{S}^2$ perpendicular to the line of sight. Similarly the volume average is insensitive to the specifics of how we transport vectors on $\mathbb{S}^2$. Of course, we are free to adopt any coordinate system that we want. However, we cannot naively equate volume and ensemble averages when the field is inhomogeneous. We have presented evidence that a spherical coordinate system allows us to extract the Kaiser signal from the components of the volume average ${}^{\mathrm{sp}}\bar{w}_i{}^j$. In contrast, the volume average in Cartesian coordinates does not necessarily replicate the ensemble average due to the nontrivial coordinate dependence of the cumulants. It is important to stress that the volume average of a tensor is generically ambiguous, and our choice of coordinates and transport determines the properties of $\bar{w}_i{}^j$. We can choose a definition that approximately respects the properties of the ensemble average $\langle w_i^j \rangle$, but ergodicity is not exactly realized except in highly idealized scenarios; Gaussian and isotropic fields, Euclidean manifolds. We have argued that it can be approximately realized for anisotropic and inhomogeneous fields, but only with careful contrivance.

We extracted the MTs from Gaussian random fields and gravitationally evolved dark matter snapshot boxes at $z = 0$, for three different fields (isotropic, plane-parallel, and spherical redshift-space distorted). We found that the plane-parallel and spherical redshift-space fields are statistically indistinguishable if the data is sufficiently distant from a central observer at $r = 0$. At cosmological distances, the inhomogeneous nature of the cumulants in spherical coordinates is negligible. Hence measurements of the MTs at redshift $z > 0.1$ from the current generation of galaxy catalogs (Alam et al. 2015) and subsequent inference of f can proceed using spherical coordinates and the plane-parallel limit being almost perfectly

respesentative of the signal. Conversely the matter distribution at low redshift $z < 0.1$ (Abazajian et al. 2009) can potentially be used to probe departures from the plane-parallel limit.

The effect of non-Gaussianity on the MTs is an order $\sim 3\%$–1% effect for the isotropic fields over the range $15\,\mathrm{Mpc} \leqslant R_{\mathrm{G}} \leqslant 45\,\mathrm{Mpc}$, manifesting as a decrease in the amplitude of the diagonal elements, and inducing a nonzero value of the coefficient of $H_1(\nu_{\mathrm{A}})$ Hermite polynomial that mildly skews the MT as a function of ν_{A}. However, in redshift space, the component of the MT parallel to the line of sight for the non-Gaussian dark matter field significantly departs from the Kaiser limit, even for large smoothing scales. The most significant effect is an amplitude decrease that is approximately $\sim 12\%$ on scales $R_{\mathrm{G}} \sim 15\,\mathrm{Mpc}$. This signal is due to large peculiar velocities along the line of sight from nonlinear regions of the density field, which can scatter particle positions over megaparsec scales. To extract the Kaiser signal from the data, we must model the nonlinear velocity component and account for this additional signal. The non-Gaussianity of the redshift-space field is also observed in the dark matter data, which indicates that, on scales $R_{\mathrm{G}} \lesssim 20\,\mathrm{Mpc}$, treating the Finger of God effect purely in terms of a suppression of the power spectrum is insufficient. Perturbative non-Gaussianity in redshift space is an important area of future study, and the MTs are necessary for studying the directional dependence of the non-Gaussian signal. The scalar Minkowski functionals, which are proportional to the trace of these quantities, contain directionally averaged information.

Although we have focused on the radial anisotropy generated by RSD, even in real space, we can expect a radially anisotropic signal. This is due to the fact that we observe tracer particles on the lightcone, and the density field evolves significantly from the beginning of the matter dominated epoch to the present. At the level of linearized perturbations, the evolution can be absorbed into a z-dependent galaxy bias, amplitude of the matter power spectrum, and the growth rate $f(z)$ in the RSD signal. In reality, the picture is more complicated on small scales, and the Minkowski functionals and tensors will exhibit systematic evolution when measured at different epochs due to non-Gaussianity induced by gravitational collapse. The non-Gaussian evolution can be potentially measured and quantified, and this will be the focus of future work. In this work, we have neglected the time dependence of $f(z)$, as this effect is tied to the evolution of the field and hence beyond the scope of our analysis. We have also neglected the potential existence of a bulk flow between observer and large-scale structure data, which would modify the expectation value of the MTs. Introducing a large-scale bulk flow is beyond the scope of this work, as it would involve the treatment of perturbations in an intrinsically anisotropic spacetime. This remains an interesting direction of further study, both within the confines of the MTs and more generally within cosmology.

The Minkowski functionals and tensors provide a method to test the fundamental assumptions on which the standard model of cosmology is based. Without the need for *a priori* assumptions, the Minkowski functionals provide a measure of the non-Gaussianity of the field as a function of scale, agnostic of the nature of non-Gaussianity. Similarly the eigenvalues of the MTs can be used to quantify the isotropy of a field without assuming the presence or absence of this symmetry property. A test of statistical homogeneity is more difficult to engineer, but coordinate dependent cumulants are a

smoking gun for inhomogeneous signals. Constructing a test of statistical homogeneity using the tensor transformation properties of the MTs is an interesting direction for future study.

isotropic or plane-parallel redshift-space distorted, then the dependence of G_2 on the second derivatives δ_{jk} does not contribute to the ensemble average; hence $\langle v_i^j \rangle$ reduces to an integral over the joint probability distribution of δ and δ_i. For an inhomogeneous field, we cannot assume this remains true and must construct the corresponding full 10×10 covariance matrix, Σ, for δ, δ_i, and δ_{jk}. For a spherically redshift-space distorted field, due to the assumed residual isotropy on the two-sphere, many off-diagonal terms are 0. The expression for Σ takes the form

$$\Sigma = \begin{pmatrix}
\langle \delta^2 \rangle & \langle \delta\delta_r \rangle & 0 & 0 & \langle \delta\delta_{rr} \rangle & 0 & 0 & \langle \delta\delta_{\theta\theta} \rangle & \langle \delta\delta_{\phi\phi} \rangle & 0 \\
\langle \delta_r\delta \rangle & \langle \delta_r^2 \rangle & 0 & 0 & \langle \delta_r\delta_{rr} \rangle & 0 & 0 & \langle \delta_r\delta_{\theta\theta} \rangle & \langle \delta_r\delta_{\phi\phi} \rangle & 0 \\
0 & 0 & \langle \delta_\theta^2 \rangle & 0 & 0 & \langle \delta_\theta\delta_{r\theta} \rangle & 0 & 0 & \langle \delta_\theta\delta_{\phi\phi} \rangle & 0 \\
0 & 0 & 0 & \langle \delta_\phi^2 \rangle & \langle \delta_\phi\delta_{rr} \rangle & 0 & \langle \delta_\phi\delta_{r\phi} \rangle & 0 & 0 & \langle \delta_\phi\delta_{\theta\phi} \rangle \\
\langle \delta_{rr}\delta \rangle & \langle \delta_{rr}\delta_r \rangle & 0 & 0 & \langle \delta_{rr}^2 \rangle & 0 & 0 & \langle \delta_{rr}\delta_{\theta\theta} \rangle & \langle \delta_{rr}\delta_{\phi\phi} \rangle & 0 \\
0 & 0 & \langle \delta_{r\theta}\delta_\theta \rangle & 0 & 0 & \langle \delta_{r\theta}^2 \rangle & 0 & 0 & \langle \delta_{r\theta}\delta_{\phi\phi} \rangle & 0 \\
0 & 0 & 0 & \langle \delta_{r\phi}\delta_\phi \rangle & 0 & 0 & \langle \delta_{r\phi}^2 \rangle & 0 & 0 & \langle \delta_{r\phi}\delta_{\theta\phi} \rangle \\
\langle \delta_{\theta\theta}\delta \rangle & \langle \delta_{\theta\theta}\delta_r \rangle & 0 & 0 & \langle \delta_{\theta\theta}\delta_{rr} \rangle & 0 & 0 & \langle \delta_{\theta\theta}^2 \rangle & \langle \delta_{\theta\theta}\delta_{\phi\phi} \rangle & 0 \\
\langle \delta_{\phi\phi}\delta \rangle & \langle \delta_{\phi\phi}\delta_r \rangle & \langle \delta_{\phi\phi}\delta_\theta \rangle & 0 & \langle \delta_{\phi\phi}\delta_{rr} \rangle & \langle \delta_{\phi\phi}\delta_{r\theta} \rangle & 0 & \langle \delta_{\phi\phi}\delta_{\theta\theta} \rangle & \langle \delta_{\phi\phi}^2 \rangle & 0 \\
0 & 0 & 0 & \langle \delta_{\theta\phi}\delta_\phi \rangle & 0 & 0 & \langle \delta_{\theta\phi}\delta_{r\phi} \rangle & 0 & 0 & \langle \delta_{\theta\phi}^2 \rangle
\end{pmatrix}. \tag{A5}$$

Appendix A
Minkowski Tensor $W_2^{0,2}$

The second independent, translation invariant MT considered in Appleby et al. (2019) is given by

$$W_2^{0,2}|_i{}^j \equiv \frac{1}{3\pi V} \int_{\partial Q} G_2 \hat{n}_i \hat{n}^j dA \tag{A1}$$

$$= \frac{1}{3\pi V} \int_V dV \, \delta_D(\delta - \delta_t) G_2 \frac{\delta_i \delta^j}{|\nabla\delta|}, \tag{A2}$$

where the scalar quantity G_2 is the mean curvature at each point of the isofield surface, and can be written as

$$G_2 = -\frac{1}{2}\nabla.\hat{\boldsymbol{n}} = -\frac{1}{2}\nabla.\left(\frac{\nabla\delta}{|\nabla\delta|}\right). \tag{A3}$$

Similarly to the $W_1^{0,2}$ case in the main body of the text, the quantity $W_2^{0,2}|_i{}^j$ can be interpreted as the volume average of the following tensor

$$v_i{}^j = \frac{1}{3\pi}\delta_D(\delta - \delta_t) G_2 \frac{\delta_i \delta^j}{|\nabla\delta|}. \tag{A4}$$

G_2 is a function of both first and second derivatives of the field. Hence when constructing the ensemble average $\langle v_i^j \rangle$, we must use a ten-dimensional multivariate probability distribution involving the field and its first and second derivatives—$X = (\delta, \delta_i, \delta_{jk})$. If the field is homogeneous and

This is the covariance matrix of the partial derivatives. If one uses covariant derivatives as random variables, then different correlations will be present. The 4×4 block in the top left corner has been calculated in the main body of the text. In this appendix, we calculate the other terms as follows:

$$\langle \delta_{rr}^2 \rangle = \left(\frac{1}{\pi^2}\right)\left(\frac{1}{10} + \frac{f}{7} + \frac{f^2}{18}\right)\int k^6 P(k, R_G)dk + \left(\frac{1}{\pi^2 r^2}\right.$$
$$\left. \times \left(\frac{4f}{5} + \frac{6f^2}{7}\right)\int k^4 P(k, R_G)dk \right.$$
$$\left. + \left(\frac{8f^2}{3\pi^2 r^6}\right)\int P(k, R_G)dk; \right.$$
$$\tag{A6}$$

$$\langle \delta_{\phi\phi}^2 \rangle = \left(\frac{r^4 \sin^4\theta}{\pi^2}\right)\left(\frac{1}{10} + \frac{f}{35} + \frac{f^2}{210}\right)\int k^6 P(k, R_G)dk$$
$$+ \left(\frac{r^2}{\pi^2}\right)\left[\frac{\sin^2\theta}{6} + \left(\frac{\sin^2\theta}{15} - \frac{6\sin^4\theta}{5}\right)f \right.$$
$$\left. + \left(\frac{\sin^2\theta}{70} + \frac{12\sin^4\theta}{35}\right)f^2\right]\int k^4 P(k, R_G)dk$$
$$+ \left(\frac{1}{\pi^2}\right)\left[\frac{-2f\sin^2\theta}{3} + \left(\frac{2\sin^2\theta}{5} + \frac{18\sin^4\theta}{5}\right)f^2\right]$$
$$\times \int k^2 P(k, R_G)dk + \frac{2f^2 \sin^2\theta}{3\pi^2 r^2}\int P(k, R_G)dk; \tag{A7}$$

$$\langle \delta_{\theta\theta}^2 \rangle = \left(\frac{r^4}{\pi^2}\right)\left(\frac{1}{10} + \frac{f}{35} + \frac{f^2}{210}\right)\int k^6 P(k, R_{\rm G})dk$$
$$+ \left(\frac{r^2}{\pi^2}\right)\left(\frac{1}{6} - \frac{17f}{15} + \frac{5f^2}{14}\right)\int k^4 P(k, R_{\rm G})dk$$
$$+ \left(\frac{1}{\pi^2}\right)\left(-\frac{2f}{3} + 4f^2\right)\int k^2 P(k, R_{\rm G})dk$$
$$+ \frac{2f^2}{3\pi^2 r^2}\int P(k, R_{\rm G})dk; \tag{A8}$$

$$\langle \delta_{r\phi}^2 \rangle = \left(\frac{r^2\sin^2\theta}{\pi^2}\right)\left(\frac{1}{30} + \frac{f}{35} + \frac{f^2}{126}\right)\int k^6 P(k, R_{\rm G})dk$$
$$+ \left(\frac{\sin^2\theta}{\pi^2}\right)\left(\frac{1}{6} + \frac{f}{5} + \frac{3f^2}{10}\right)\int k^4 P(k, R_{\rm G})dk$$
$$+ \left(\frac{\sin^2\theta}{\pi^2 r^2}\right)\left(\frac{2f}{3} + \frac{4f^2}{5}\right)\int k^2 P(k, R_{\rm G})dk$$
$$+ \frac{2f^2\sin^2\theta}{3\pi^2 r^4}\int P(k, R_{\rm G})dk; \tag{A9}$$

$$\langle \delta_{r\theta}^2 \rangle = \left(\frac{r^2}{\pi^2}\right)\left(\frac{1}{30} + \frac{f}{35} + \frac{f^2}{126}\right)\int k^6 P(k, R_{\rm G})dk$$
$$+ \left(\frac{1}{\pi^2}\right)\left(\frac{1}{6} + \frac{f}{5} + \frac{3f^2}{10}\right)\int k^4 P(k, R_{\rm G})dk$$
$$+ \left(\frac{1}{\pi^2 r^2}\right)\left(\frac{2f}{3} + \frac{4f^2}{5}\right)\int k^2 P(k, R_{\rm G})dk$$
$$+ \frac{2f^2}{3\pi^2 r^4}\int P(k, R_{\rm G})dk; \tag{A10}$$

$$\langle \delta_{\theta\phi}^2 \rangle = \left(\frac{r^4\sin^2\theta}{\pi^2}\right)\left(\frac{1}{30} + \frac{f}{105} + \frac{f^2}{630}\right)\int k^6 P(k, R_{\rm G})dk$$
$$+ \left(\frac{r^2}{\pi^2}\right)\left[\left(\frac{1}{6} - \frac{\sin^2\theta}{6}\right) + \left(\frac{1}{15} - \frac{7\sin^2\theta}{15}\right)f\right.$$
$$+ \left.\left(\frac{1}{70} + \frac{\sin^2\theta}{10}\right)f^2\right]\int k^4 P(k, R_{\rm G})dk$$
$$+ \left(\frac{1}{\pi^2}\right)\left[\left(-\frac{2}{3} + \frac{2\sin^2\theta}{3}\right)f + \left(\frac{2}{5} + \frac{4\sin^2\theta}{5}\right)f^2\right]$$
$$\times \int k^2 P(k, R_{\rm G})dk$$
$$+ \left(\frac{f^2}{\pi^2 r^2}\right)\left(\frac{2}{3} - \frac{2\sin^2\theta}{3}\right)\int P(k, R_{\rm G})dk; \tag{A11}$$

$$\langle \delta_{rr}\delta_{\phi\phi} \rangle = \left(\frac{r^2\sin^2\theta}{\pi^2}\right)\left(\frac{1}{30} + \frac{f}{35} + \frac{f^2}{126}\right)\int k^6 P(k, R_{\rm G})dk$$
$$+ \left(\frac{\sin^2\theta}{\pi^2}\right)\left(\frac{2f}{15} + \frac{2f^2}{7}\right)\int k^4 P(k, R_{\rm G})dk$$
$$+ \left(\frac{\sin^2\theta}{\pi^2 r^2}\right)\left(\frac{2f}{3} + \frac{4f^2}{5}\right)\int k^2 P(k, R_{\rm G})dk$$
$$- \left(\frac{4f^2\sin^2\theta}{3\pi^2 r^4}\right)\int P(k, R_{\rm G})dk; \tag{A12}$$

$$\langle \delta_{rr}\delta_{\theta\theta} \rangle = \left(\frac{r^2}{\pi^2}\right)\left(\frac{1}{30} + \frac{f}{35} + \frac{f^2}{126}\right)\int k^6 P(k, R_{\rm G})dk$$
$$+ \left(\frac{1}{\pi^2}\right)\left(\frac{2f}{15} + \frac{2f^2}{7}\right)\int k^4 P(k, R_{\rm G})dk$$
$$+ \left(\frac{1}{\pi^2 r^2}\right)\left(\frac{2f}{3} + \frac{4f^2}{5}\right)\int k^2 P(k, R_{\rm G})dk$$
$$- \left(\frac{4f^2}{3\pi^2 r^4}\right)\int P(k, R_{\rm G})dk; \tag{A13}$$

$$\langle \delta_{r\theta}\delta_{\phi\phi} \rangle = \left(\frac{r\sin 2\theta}{\pi^2}\right)\left(\frac{-1}{12} - \frac{f}{30} - \frac{f^2}{140}\right)$$
$$\times \int k^4 P(k, R_{\rm G})dk + \left(\frac{f^2\sin 2\theta}{3\pi^2 r^3}\right)\int P(k, R_{\rm G})dk; \tag{A14}$$

$$\langle \delta_{r\phi}\delta_{\theta\phi} \rangle = \left(\frac{r\sin 2\theta}{\pi^2}\right)\left(\frac{1}{12} + \frac{f}{30} + \frac{f^2}{140}\right)$$
$$\times \int k^4 P(k, R_{\rm G})dk - \left(\frac{f^2\sin 2\theta}{3\pi^2 r^3}\right)\int P(k, R_{\rm G})dk; \tag{A15}$$

$$\langle \delta\delta_r \rangle = \left(\frac{-2f^2}{3\pi^2 r^3}\right)\int P(k)dk; \tag{A16}$$

$$\langle \delta\delta_{rr} \rangle = \left(\frac{1}{\pi^2}\right)\left(-\frac{1}{6} - \frac{f}{5} - \frac{f^2}{14}\right)\int k^4 P(k, R_{\rm G})dk$$
$$+ \left(\frac{1}{\pi^2 r^2}\right)\left(-\frac{2f}{3} - \frac{4f^2}{5}\right)\int k^2 P(k, R_{\rm G})dk$$
$$+ \left(\frac{4f^2}{3\pi^2 r^4}\right)\int P(k, R_{\rm G})dk; \tag{A17}$$

$$\langle \delta_r\delta_{rr} \rangle = \left(\frac{1}{\pi^2 r^3}\right)\left(-\frac{2f}{3} - \frac{4f^2}{5}\right)$$
$$\times k^2 P(k, R_{\rm G})dk - \left(\frac{4f^2}{3\pi^2 r^5}\right)\int P(k, R_{\rm G})dk; \tag{A18}$$

$$\langle \delta_{r\theta}\delta_\theta \rangle = \left(\frac{r}{\pi^2}\right)\left(\frac{1}{6} + \frac{f}{15} + \frac{f^2}{70}\right)$$
$$\times k^4 P(k, R_{\rm G})dk - \left(\frac{2f^2}{3\pi^2 r^3}\right)\int P(k, R_{\rm G})dk; \tag{A19}$$

$$\langle \delta_{r\phi}\delta_\phi \rangle = \left(\frac{r\sin^2\theta}{\pi^2}\right)\left(\frac{1}{6} + \frac{f}{15} + \frac{f^2}{70}\right)$$
$$\times k^4 P(k, R_{\rm G})dk - \left(\frac{2f^2\sin^2\theta}{3\pi^2 r^3}\right)\int P(k, R_{\rm G})dk; \tag{A20}$$

$$\langle \delta_{\theta\theta}\delta \rangle = \left(\frac{r^2}{\pi^2}\right)\left(-\frac{1}{6} - \frac{f}{15} - \frac{f^2}{70}\right)\int k^4 P(k, R_{\rm G})dk$$
$$+ \left(\frac{1}{\pi^2}\right)\left(\frac{2f}{3} - \frac{2f^2}{5}\right)\int k^2 P(k, R_{\rm G})dk$$
$$- \left(\frac{2f^2}{3\pi^2 r^2}\right)\int P(k, R_{\rm G})dk; \tag{A21}$$

$$\langle\delta_{\phi\phi}\delta\rangle = \left(\frac{r^2\sin^2\theta}{\pi^2}\right)\left(-\frac{1}{6} - \frac{f}{15} - \frac{f^2}{70}\right)\int k^4 P(k, R_G)dk$$
$$+ \left(\frac{\sin^2\theta}{\pi^2}\right)\left(\frac{2f}{3} - \frac{2f^2}{5}\right)\int k^2 P(k, R_G)dk$$
$$- \left(\frac{2f^2\sin^2\theta}{3\pi^2 r^2}\right)\int P(k, R_G)dk; \tag{A22}$$

$$\langle\delta_{\theta\theta}\delta_r\rangle = \left(\frac{r}{\pi^2}\right)\left(-\frac{1}{6} - \frac{f}{15} - \frac{f^2}{70}\right)\int k^4 P(k, R_G)dk$$
$$+ \left(\frac{2f^2}{3\pi^2 r^3}\right)\int P(k, R_G)dk; \tag{A23}$$

$$\langle\delta_{\phi\phi}\delta_r\rangle = \left(\frac{r\sin^2\theta}{\pi^2}\right)\left(-\frac{1}{6} - \frac{f}{15} - \frac{f^2}{70}\right)\int k^4 P(k, R_G)dk$$
$$+ \left(\frac{2f^2\sin^2\theta}{3\pi^2 r^3}\right)\int P(k, R_G)dk; \tag{A24}$$

$$\langle\delta_{\phi\phi}\delta_\theta\rangle = \left(\frac{r^2\sin 2\theta}{\pi^2}\right)\left(-\frac{1}{12} - \frac{f}{30} - \frac{f^2}{140}\right)$$
$$\times \int k^4 P(k, R_G)dk + \left(\frac{\sin 2\theta}{\pi^2}\right)\left(\frac{f}{3} - \frac{f^2}{5}\right)$$
$$\times \int k^2 P(k, R_G)dk$$
$$- \left(\frac{f^2\sin 2\theta}{3\pi^2 r^2}\right)\int P(k, R_G)dk; \tag{A25}$$

$$\langle\delta_{\theta\theta}\delta_\phi\rangle = \left(\frac{r^2\sin 2\theta}{\pi^2}\right)\left(\frac{1}{12} + \frac{f}{30} + \frac{f^2}{140}\right)\int k^4 P(k, R_G)dk$$
$$+ \left(\frac{\sin 2\theta}{\pi^2}\right)\left(-\frac{f}{3} + \frac{f^2}{5}\right)\int k^2 P(k, R_G)dk$$
$$+ \left(\frac{f^2\sin 2\theta}{3\pi^2 r^2}\right)\int P(k, R_G)dk. \tag{A26}$$

These are the correlations between partial derivatives of the field, although covariant derivatives can be used instead. If we take the limit $r \to \infty$, then the covariance matrix reduces to the plane-parallel limit. Hence similar to the main body of the text, if the field is sufficiently distant from the observer at $r = 0$, the ensemble average $\langle v_i^j \rangle$ is well approximated by the plane-parallel result in Appleby et al. (2019). More concretely, the dimensionless terms $\sigma_{-1}^2/(r^6\sigma_2^2)$, $\sigma_1^2/(r^2\sigma_2^2)$, $\sigma_0^2/(r^4\sigma_2^2)$ must all be negligible to satisfy the plane-parallel limit.

The volume average of v_i^j in a spherical basis is given by

$$^{\mathrm{sp}}\bar{v}_i^{\ j} = \frac{1}{3\pi V}\sum_{m,n,p}\Delta^3\delta_D(\tilde{\delta}_{\{m,n,p\}} - \delta_t)$$
$$\times G_{2\,\{m,n,p\}}\frac{{}^\gamma\tilde{\delta}_{i\{m,n,p\}}\,{}^\gamma\tilde{\delta}^{\,j}_{\{m,n,p\}}}{|\nabla\tilde{\delta}_{\{m,n,p\}}|}. \tag{A27}$$

This is straightforward to construct; the only complication beyond $^{\mathrm{sp}}\bar{w}_i^{\ j}$ is that we must additionally estimate G_2 at each pixel using Equation (A3). Since G_2 is a scalar quantity, we use Cartesian coordinates and a simple second-order accurate finite difference scheme for the first and second derivatives to reconstruct $G_{2\,\{m,n,p\}}$ at each pixel.

In Figure 11, we present the components of the MT $\bar{v}_i^{\ j}$ from the Quijote $z = 0$ snapshot boxes, smoothed with scale $R_G = 20$ Mpc as a function of ν (left panel) and ν_A (right panel). The color scheme matches Figure 7 in the main body of the text. All off-diagonal components are consistent with 0 and not plotted. The RSD signal is present, with the (θ, θ), (ϕ, ϕ) components systematically lower in amplitude compared to the real-space statistics (see light hollow diamonds). The radial component (red filled diamonds) is only marginally higher than the isotropic components—this is due to the same Finger of God effect observed in the main body of the text (see Section 6.2).

In Figure 12, we present the amplitude of $\bar{v}_i^{\ j}$ defined as the coefficient of the H_1 coefficient:

$$B|_i^{\ j} = \frac{1}{\sqrt{2\pi}}\int_{-\nu_{\max}}^{\nu_{\max}}\bar{v}_i^{\ j}(\nu_A)H_1(\nu_A)d\nu_A, \tag{A28}$$

and the additional Hermite polynomial coefficients

$$b_0|_i^{\ j} = \frac{1}{\sqrt{2\pi}}\int_{-\nu_{\max}}^{\nu_{\max}}\bar{v}_i^{\ j}(\nu_A)H_0(\nu_A)d\nu_A, \tag{A29}$$

$$b_2|_i^{\ j} = \frac{1}{2\sqrt{2\pi}}\int_{-\nu_{\max}}^{\nu_{\max}}\bar{v}_i^{\ j}(\nu_A)H_2(\nu_A)d\nu_A. \tag{A30}$$

The color scheme is the same as in Figure 8. Qualitatively we observe the same behavior for $W_2^{0,2}$ as $W_1^{0,2}$; but here it is more pronounced. Both the isotropic and spherically redshift-space distorted fields are significantly affected by the non-Gaussianity of the Quijote fields for scales $R_G \leqslant 35$ Mpc, and the (r, r) component in redshift space most significantly departs from the Gaussian limit (see top panels, red diamonds and error bars). The redshift-space Gaussian and plane-parallel limit of the amplitudes are given by

$$^{\mathrm{pp}}B_G|_x^{\ x} = \frac{3}{2}\sqrt{\frac{\pi}{2}}A_0^2$$
$$\times \left[\frac{(\lambda^2 - 2)(\lambda^2 - 1)^{1/2} + \lambda^4\tan^{-1}\sqrt{\lambda^2 - 1}}{(\lambda^2 - 1)^{3/2}}\right], \tag{A31}$$

$$^{\mathrm{pp}}B_G|_y^{\ y} = {}^{\mathrm{pp}}B_G|_x^{\ x}, \tag{A32}$$

$$^{\mathrm{pp}}B_G|_z^{\ z} = 3\sqrt{\frac{\pi}{2}}A_0^2$$
$$\times \left[\frac{\lambda^2[(\lambda^2 - 1)^{1/2} + (\lambda^2 - 2)\tan^{-1}\sqrt{\lambda^2 - 1}]}{(\lambda^2 - 1)^{3/2}}\right], \tag{A33}$$

and the isotropic Gaussian limit is

$$^{\mathrm{re}}B_G|_x^{\ x} = {}^{\mathrm{re}}B_G|_y^{\ y} = {}^{\mathrm{re}}B_G|_z^{\ z} = \frac{\sigma_1^2}{27\pi\sqrt{2\pi}\,\sigma_0^2}. \tag{A34}$$

The non-Gaussian coefficients $b_0|_i^j$ and $b_2|_i^j$ remain small even on relatively small scales $R_G \gtrsim 15$ Mpc.
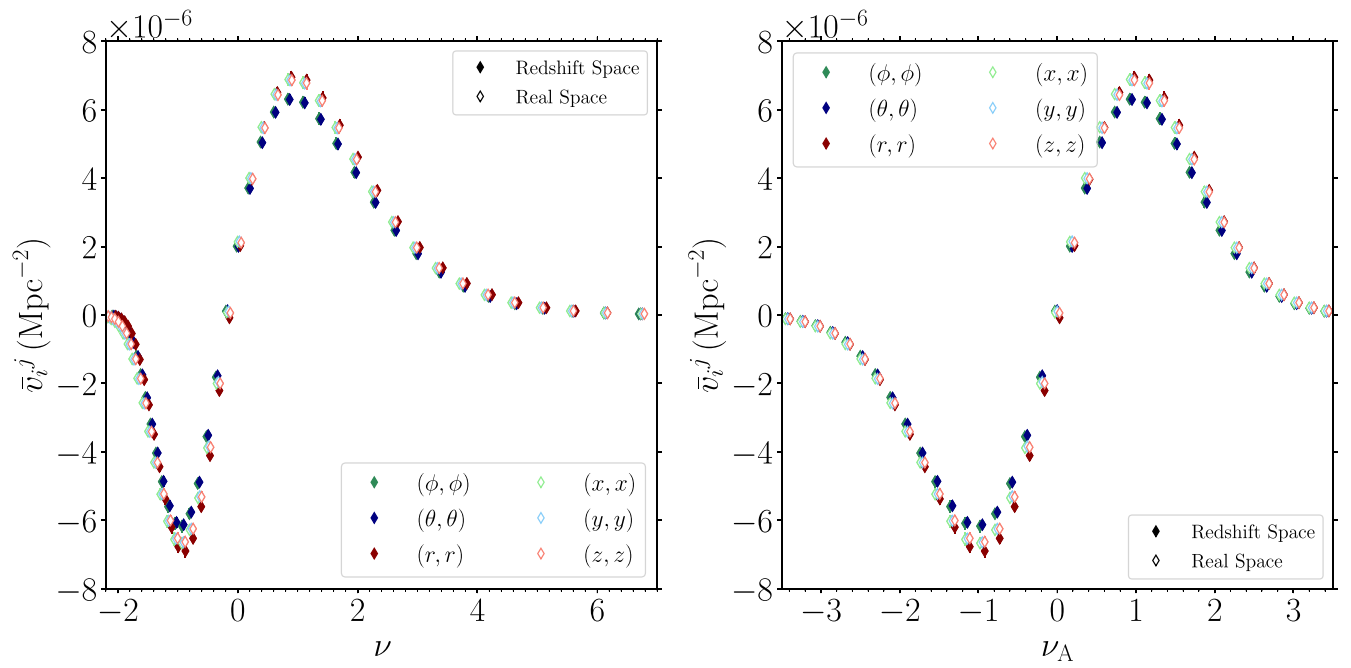
Figure 11. Components of the Minkowski tensor $\bar{v}_i^{\ j}$ extracted from the Quijote simulations in real space (open diamonds), and spherical redshift space (filled diamonds) as a function of normalized threshold ν (left panel) and rescaled threshold ν_A (right panel). The off-diagonal elements are consistent with 0 and not plotted. The fields have been smoothed with scale $R_G = 20$ Mpc.
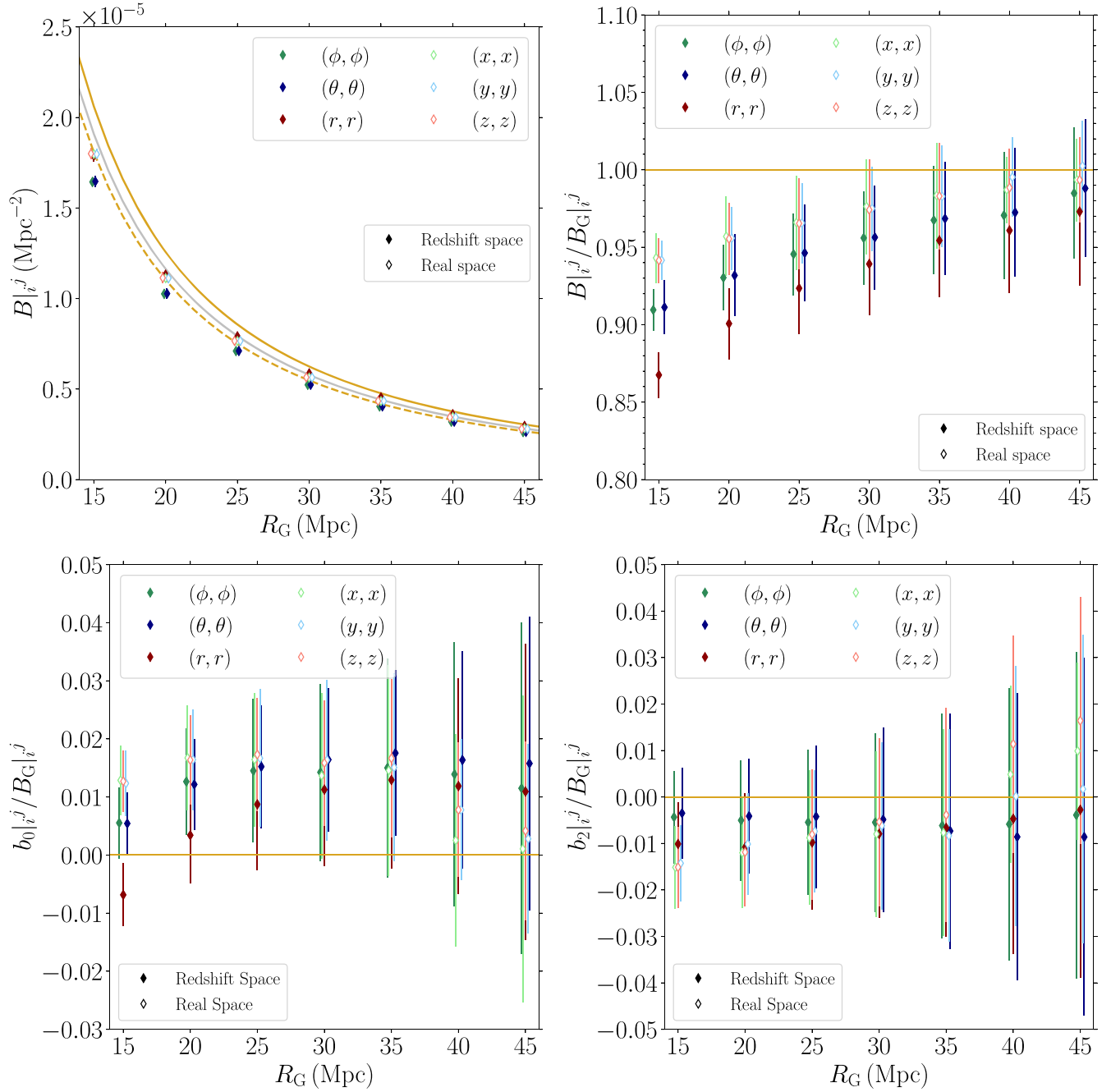
Figure 12. $B|_i^{|j}$ (top left), $b_0|_i^{|j}$ (lower left), and $b_2|_i^{|j}$ (lower right) quantities as defined in Equations (A28), (A29), and (A30) measured from $N_{\rm real} = 50$ Quijote simulations, at $z = 0$, in real and redshift space. The solid/dashed gold lines in the top left panel represent the expectation values of the radial/angular components for a Gaussian field in the plane-parallel limit, and the silver line is the isotropic Gaussian expectation value. The top right panel shows the fractional difference between the Quijote measurements of $B|_i^{|j}$ and the Gaussian limit of this quantity in real and redshift space.

Appendix B
Rotation of Basis Vectors Relative to a Great Arc

In the main body of the paper, we constructed an algorithm to describe the rotation of a vector under geodesic transport to a different location on the two-sphere. In this appendix, we present the rotation of the spherical basis vectors explicitly using a simple geometric prescription. Starting with the unit sphere, we select two points on the sphere defined with $\mathbb{R}^3$ unit vectors $\hat{u}$ and $\hat{v}$. To parameterize the great arc that passes through these two points, we introduce the vectors $\hat{m} = \hat{u} \times \hat{v}/|\hat{u} \times \hat{v}|$, and $\hat{n} = \hat{m} \times \hat{u}/|\hat{m} \times \hat{u}|$. The unit vectors $\hat{u}$, $\hat{m}$, and $\hat{n}$ are mutually orthogonal, and $\hat{u}$, $\hat{n}$ form a basis

in the plane in which the great circle is defined. Any position on the great arc can then be represented parametrically with the vector

$$\hat{R} = \hat{u} \cos t + \hat{n} \sin t, \tag{B1}$$

for $0 < t \leqslant 2\pi$. The tangent vector to the great arc is

$$\hat{T} = -\hat{u} \sin t + \hat{n} \cos t. \tag{B2}$$

Each point on the great arc, specified by the vector $\hat{R}$, can be described using the angles θ, ϕ in a spherical coordinate system, and we can then define the spherical basis vectors in
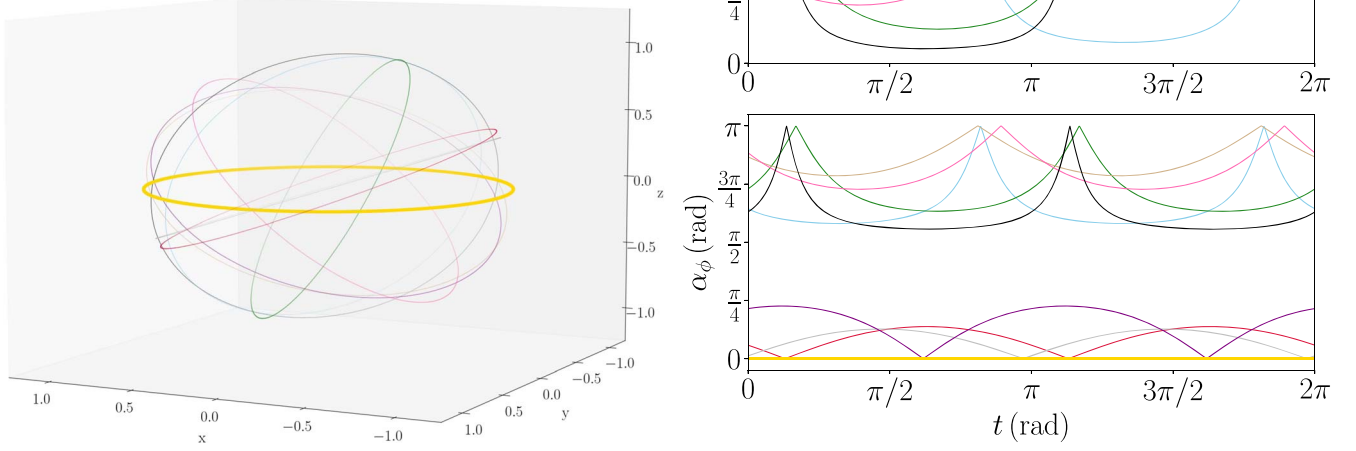
Figure 13. Left panel: a collection of randomly selected great arcs on the unit sphere. The thick gold line is the great arc that coincides with the equator in the coordinate system adopted. Right panel: the angle between $\boldsymbol{e}_\theta$ and $\hat{T}$ (top panel) and $\boldsymbol{e}_\phi$ and $\hat{T}$ (bottom panel), as a function of great arc parameter t. The colors match the great arcs in the left panel.

the usual way:

$$\boldsymbol{e}_r = \sin\theta\cos\phi\,\boldsymbol{e}_x + \sin\theta\sin\phi\,\boldsymbol{e}_y + \cos\theta\,\boldsymbol{e}_z; \qquad (B3)$$

$$\boldsymbol{e}_\theta = \cos\theta\cos\phi\,\boldsymbol{e}_x + \cos\theta\sin\phi\,\boldsymbol{e}_y - \sin\theta\,\boldsymbol{e}_z; \qquad (B4)$$

$$\boldsymbol{e}_\phi = -\sin\phi\,\boldsymbol{e}_x + \cos\phi\,\boldsymbol{e}_y. \qquad (B5)$$

The dot products $\hat{T}.\boldsymbol{e}_\theta$, $\hat{T}.\boldsymbol{e}_\phi$ then represent the angle rotation of the spherical basis vectors relative to the great arc tangent along the path. This is the rotation that is accounted for in the main body of the text, when summing vector fields at different locations on the manifold. Parallel transport preserves the orientation of a tangent space relative to $\hat{T}$, so after geodesic transport, the components of a vector in the basis $\boldsymbol{e}_\theta$, $\boldsymbol{e}_\phi$ are rotated. Conversely the dot product $\hat{T}.\boldsymbol{e}_r$ is always 0, and the components of a vector parallel to $\boldsymbol{e}_r$ are preserved. If the great arc lies on the equator of the sphere, then the basis vectors do not rotate with respect to the great arc tangent vector.

We present $N = 10$ great arcs defined by selecting $\hat{u}$, $\hat{v}$ randomly in the left panel of Figure 13. The thick gold arc lies on the equator. The corresponding rotation angles $\alpha_\theta = \cos^{-1}(\hat{T}.\boldsymbol{e}_\theta)$, and $\alpha_\phi = \cos^{-1}(\hat{T}.\boldsymbol{e}_\phi)$, as a function of the arc parameter t, are presented in the right panel of Figure 13. Only when the great arc aligns with the coordinate basis is there no relative rotation of the tangent space (see gold lines). There are two points on each great arc at which the path is perpendicular to $\boldsymbol{e}_\theta$, and hence $\hat{T}$ either aligns or antialigns with $\boldsymbol{e}_\phi$, depending on the direction of the arc tangent vector. This is the origin of the dichotomy observed in the α_ϕ panel. Note that the vectors return to their original orientation if transported along the entire great arc.

Figure 13 elucidates the origin of the rotation of the angular components of $\tilde{\delta}_i$ under the process of parallel transport along great arcs, described in the main body of the text. Great arc transport preserves the angle between $\tilde{\delta}_i$ and the tangent vector to the curve. In contrast, here we explicitly show that the angle

between the tangent vector and angular basis vectors, $\boldsymbol{e}_\theta$ and $\boldsymbol{e}_\phi$, is not constant along the curve.

Appendix C
Useful Relations

We provide some useful identities regarding the spherical Bessel functions and other functions that are used in the paper. Some of these can be found in standard textbooks (Abramowitz & Stegun 1965):

$$\sum_{m=-\ell}^{\ell} Y_{\ell m}(\hat{s}_1) Y_{\ell m}^*(\hat{s}_2) = \frac{2\ell+1}{4\pi}\mathcal{L}_\ell(\hat{s}_1.\hat{s}_2), \qquad (C1)$$

$$\sum_{m=-\ell}^{\ell} \frac{\partial Y_{\ell m}(\theta,\phi)}{\partial\phi}\frac{\partial Y_{\ell m}^*(\theta,\phi)}{\partial\phi} = \frac{(2\ell+1)\ell(\ell+1)}{8\pi}\sin^2\theta, \qquad (C2)$$

$$\sum_{m=-\ell}^{\ell} \frac{\partial Y_\ell^{m*}(\theta,\phi)}{\partial\theta}\frac{\partial Y_\ell^m(\theta,\phi)}{\partial\theta} = \frac{(2\ell+1)\ell(\ell+1)}{8\pi}, \qquad (C3)$$

$$\sum_{m=-\ell}^{\ell} \frac{\partial^2 Y_\ell^{m*}(\theta,\phi)}{\partial\phi^2}\frac{\partial^2 Y_\ell^m(\theta,\phi)}{\partial\phi^2} = \frac{(2\ell+1)\ell(\ell+1)}{8\pi}$$
$$\times \sin^2\theta\left[\frac{3\sin^2\theta}{4}\left(\ell(\ell+1)+\left(1-\frac{3\sin^2\theta}{2}\right)\right)\right], \qquad (C4)$$

$$\sum_{m=-\ell}^{\ell} \frac{\partial^2 Y_\ell^{m*}(\theta,\phi)}{\partial\theta^2}\frac{\partial^2 Y_\ell^m(\theta,\phi)}{\partial\theta^2}$$
$$= \frac{(2\ell+1)\ell(\ell+1)}{8\pi}\left[\frac{3}{4}\ell(\ell+1)-\frac{1}{2}\right]. \qquad (C5)$$

These can be derived using the general result;

$$P_\ell(\cos\gamma) = \frac{4\pi}{2\ell+1}\sum_{m=-\ell}^{\ell} Y_\ell^{m*}(\theta',\phi')Y_\ell^m(\theta,\phi), \qquad (C6)$$

where

$$\cos\gamma = \cos\theta\cos\theta' + \sin\theta\sin\theta'\cos(\phi - \phi'), \qquad (C7)$$

along with the differential equation that the Legendre polynomial solves—

$$(1 - x^2)P''_\ell(x) - 2xP'_\ell(x) + \ell(\ell + 1)P_\ell(x) = 0, \qquad (C8)$$

and the normalization $P_\ell(1) = 1$. Taking derivatives of Equation (C6) w.r.t. ϕ, ϕ', θ, θ', and then taking the limit $\theta \to \theta'$, $\phi \to \phi'$, and $x = \cos\gamma \to 1$ yields results such as Equations (C2), (C3).

We also have the following relation for the spherical Bessel function of the first kind, j_ℓ,

$$\sum_{\ell=0}^{\infty}(2\ell + 1)[j_\ell^{(p)}(x)]^2 = \frac{1}{2p + 1}, \qquad (C9)$$

where the (p) superscript denotes the pth derivative of the spherical Bessel function with respect to its argument. Also important are the following relations:

$$\sum_{\ell=0}^{\infty}(2\ell + 1)\ell(\ell + 1)j_\ell^2(x) = \frac{2x^2}{3}, \qquad (C10)$$

$$\sum_{\ell=0}^{\infty}(2\ell + 1)\ell(\ell + 1)[j'_\ell(x)]^2 = \frac{2}{3} + \frac{2}{15}x^2, \qquad (C11)$$

$$\sum_{\ell=0}^{\infty}(2\ell + 1)\ell(\ell + 1)[j''_\ell(x)]^2 = \frac{8}{15} + \frac{2x^2}{35}. \qquad (C12)$$

The j_ℓ functions satisfy the equation

$$\ell(\ell + 1)j_\ell(x) = x^2 j''_\ell(x) + 2xj'_\ell(x) + x^2 j_\ell(x), \qquad (C13)$$

which can be differentiated w.r.t. x twice to give

$$\ell(\ell + 1)j''_\ell(x) = x^2 j''''_\ell(x) + 6xj'''_\ell(x)$$
$$+ (x^2 + 6)j''_\ell(x) + 4xj'_\ell(x) + 2j_\ell(x). \qquad (C14)$$

In Section 6, when reconstructing the MTs numerically, we transform between Cartesian and spherical coordinate systems. We adopt the standard angle conventions such that the conversion from Cartesian to radial gradients is

$$\frac{\partial\Omega}{\partial r} = \sin\theta\cos\phi\frac{\partial\Omega}{\partial x} + \sin\theta\sin\phi\frac{\partial\Omega}{\partial y} + \cos\theta\frac{\partial\Omega}{\partial z}. \qquad (C15)$$

To define volume averages in Section 6, we rotate vectors on the two-sphere. To do so, we define $\hat{\boldsymbol{m}}$ as the unit vector pointing to a position on the manifold at which the $\delta_D(\tilde{\delta}_{[m,n,p]} - \delta_t) \neq 0$, and $\hat{\boldsymbol{a}}$ is the unit vector pointing to a fiducial point at which we take the volume average of w_i^j, then the unit quaternion $q = q_0 + \boldsymbol{q}$ with elements

$$q_0 = \cos\frac{\theta}{2}, \qquad \boldsymbol{q} = \frac{\hat{\boldsymbol{m}} \times \hat{\boldsymbol{a}}}{|\hat{\boldsymbol{m}} \times \hat{\boldsymbol{a}}|}\sin\frac{\theta}{2}, \qquad (C16)$$

is used to rotate the gradient vector sampled at $[m, n, p]$ to $[a, b, c]$, where $\cos\theta = \hat{\boldsymbol{m}}.\hat{\boldsymbol{a}}$. The complex conjugate is $q^* = q_0 - \boldsymbol{q}$, and the rotation operator acting on an arbitrary vector $\boldsymbol{v}$ can be written as

$$qvq^* = (q_0^2 - |\boldsymbol{q}|^2)\boldsymbol{v} + 2(\boldsymbol{q}.\boldsymbol{v})\boldsymbol{q} + 2q_0(\boldsymbol{q} \times \boldsymbol{v}). \qquad (C17)$$

Finally, we present an example of a Quijote snapshot box in Figure 14. In the top left panel, we exhibit the point distribution of the snapshot box. We place an observer in the center of the box, and perturb all particle positions according to their radial velocity in the $\boldsymbol{e}_r$ direction relative to the observer. We then smooth the field in Fourier space, generating a zero mean, unit variance continuous field $\tilde{\delta}$ (top right panel). We mask regions of the box, keeping only pixels at radial separation $100\,\text{Mpc} < r < 630\,\text{Mpc}$, and from these pixels, we apply the discretized delta function to select pixels that are approximately equal to some threshold value. At these pixels, we sample the gradient of the density field. An example of the pixel sampling, for threshold value $\tilde{\delta} = 2.5$, is presented in the lower left panel of Figure 14. We transport these vectors to a common point on the manifold using great arc transport and radial translation, and taking the volume average at that point. In the lower right panel, we present an alternative numerical approach in which a triangulated mesh of constant field value is generated—$\tilde{\delta} = 2.5$ in this example; and the normals to the boundary are constructed. For the smoothing scales and resolutions utilized in this work, the two methods yield statistically equivalent results.
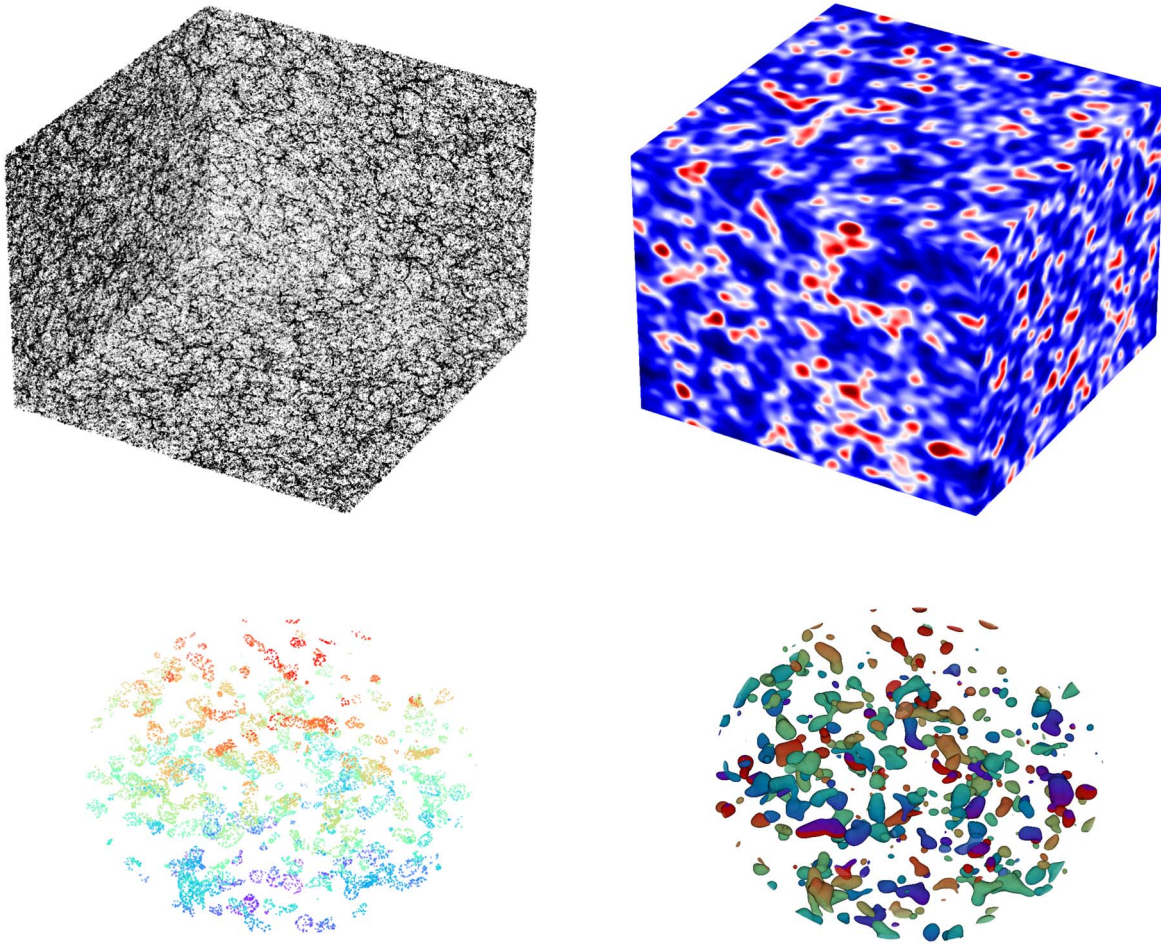
Figure 14. Representation of the point distribution of a quijote dark matter snapshot box (top left), the corresponding field Gaussian smoothed with scale $R_G = 20$ Mpc (top right). The discretized delta function method selects a subset of pixels from which the field gradient is sampled. Pixel sampling is shown in the lower left panel, taking threshold $\tilde{\delta} = 2.5$. An alternative numerical algorithm can be adopted—generating a triangulated mesh (lower right panel), from which normals can be constructed. The two approaches yield statistically equivalent results for the choice of smoothing scales and resolutions considered in this work. The colors in the lower panels are for image clarity only.

ORCID iDs

Joby P. Kochappan ⓘ https://orcid.org/0000-0001-8849-3986
Changbom Park ⓘ https://orcid.org/0000-0001-9521-6397

References

Abazajian, K. N., Adelman-McCarthy, J. K., Agüeros, M. A., et al. 2009, ApJS, 182, 543
Aluri, P. K., Cea, P., Chingangbam, P., et al. 2022, arXiv:2207.05765
Abramowitz, M., & Stegun, I. A. 1965, Handbook of Mathematical Functions with Formulas, Graphs and Mathematical Tables (New York: Dover Publications, Inc.)
Adler, R. 1981, The Geometry of Random Fields (New York: Wiley)
Alam, S., Albareti, F. D., Prieto, C. A., et al. 2015, ApJS, 219, 12
Alesker, S. 1999, Geometriae Dedicata, 74, 241
Appleby, S., Chingangbam, P., Park, C., et al. 2018a, ApJ, 858, 87
Appleby, S., Chingangbam, P., Park, C., Yogendran, K. P., & Joby, P. K. 2018b, ApJ., 863, 200
Appleby, S., Kochappan, J. P., Chingangbam, P., & Park, C. 2019, ApJ, 887, 128
Appleby, S., Park, C., Hong, S. E., et al. 2021, ApJ, 907, 75
Becker, J., Grun, G., Seemann, R., et al. 2003, NatMa, 2, 59
Beisbart, C., Buchert, T., & Wagner, H. 2001a, Phy, A293, 592
Beisbart, C., Dahlke, R., Mecke, K., & Wagner, H. 2002, LNP, 600, 238
Beisbart, C., Valdarnini, R., & Buchert, T. 2001b, A&A, 379, 412
Beutler, F., Saito, S., Seo, H.-J., et al. 2014, MNRAS, 443, 1065
Bharadwaj, S., Sahni, V., Sathyaprakash, B. S., Shandarin, S. F., & Yess, C. 2000, ApJ, 528, 21

Bonvin, C., & Durrer, R. 2011, PhRvD, 84, 063505
Buchert, T., France, M. J., & Steiner, F. 2017, CQGra, 34, 094002
Castorina, E., & White, M. 2018, MNRAS, 476, 4403
Chingangbam, P., Goyal, P., Yogendran, K. P., & Appleby, S. 2021, PhRv, 104, 123516
Chingangbam, P., Yogendran, K. P., & K., J. P. 2017, JCAP, 12, 023
Codis, S., Pichon, C., Pogosyan, D., Bernardeau, F., & Matsubara, T. 2013, MNRAS, 435, 531
Desjacques, V., & Sheth, R. K. 2010, PhRvD, 81, 023526
Doroshkevich, A. G. 1970, Ap, 6, 320
Feldbrugge, J., van Engelen, M., van de Weygaert, R., Pranav, P., & Vegter, G. 2019, JCAP, 1909, 052
Fisher, K. B. 1995, ApJ, 448, 494
Ganesan, V., & Chingangbam, P. 2017, JCAP, 1706, 023
Gay, C., Pichon, C., & Pogosyan, D. 2012, PhRvD, 85, 023011
Gott, J. R. III., Park, C., Juszkiewicz, R., et al. 1990, ApJ, 352, 1
Gott, J. R. III., Weinberg, D. H., & Melott, A. L. 1987, ApJ, 319, 1
Gott, J. R. III., Dickinson, M., & Melott, A. L. 1986, ApJ, 306, 341
Goyal, P., & Chingangbam, P. 2021, JCAP, 2021, 006
Goyal, P., Chingangbam, P., & Appleby, S. 2020, JCAP, 2020, 020
Gramann, M. 1993, ApJ, 405, 449
Hamilton, A. J. S. 1992, ApJL, 385, L5
Hamilton, A. J. S. 1997, in Ringberg Workshop on Large Scale Structure, Vol. 231 (Dordrecht: Kluwer Academic), 185
Hamilton, A. J. S., & Culhane, M. 1996, MNRAS, 278, 73
Hamilton, J. S. A., Gott, J. R., & Weinberg, D. 1986, ApJ, 309, 1
Hikage, C., Coles, P., Grossi, M., et al. 2008, MNRAS, 385, 1613
Hikage, C., & Yamamoto, K. 2013, JCAP, 08, 019
Hug, D., Schneider, R., & Schuster, R. 2008, St. Petersburg Math. J., 19, 137
Jackson, J. C. 1972, MNRAS, 156, 1P

Jennings, E., Baugh, C. M., & Pascoli, S. 2010, ApJL, 727, L9
Jennings, E., Baugh, C. M., & Pascoli, S. 2011, MNRAS, 410, 2081
Joby, P. K., Chingangbam, P., Ghosh, T., Ganesan, V., & Ravikumar, C. D. 2019, JCAP, 1901, 009
Juszkiewicz, R., Fisher, K. B., & Szapudi, I. 1998, ApJL, 504, L1
Kaiser, N. 1987, MNRAS, 227, 1
Kapahtia, A., Chingangbam, P., & Appleby, S. 2019, JCAP, 09, 053
Kapahtia, A., Chingangbam, P., Appleby, S., & Park, C. 2018, JCAP, 1810, 011
Kapahtia, A., Chingangbam, P., Ghara, R., Appleby, S., & Choudhury, T. R. 2021, JCAP, 2021, 026
Kim, Y.-R., Choi, Y.-Y., Kim, S. S., et al. 2014, ApJS, 212, 22
Klatt, M. A., Hörmann, M., & Mecke, K. 2022, JSMTE, 2022, 043301
Klatt, M. A., Last, G., Mecke, K., et al. 2016, arXiv:1606.07653
Kochappan, J. P., Sen, A., Ghosh, T., Chingangbam, P., & Basak, S. 2021, PhRvD, 103, 123523
Kwan, J., Lewis, G. F., & Linder, E. V. 2012, ApJ, 748, 78
Lim, E. A., & Simon, D. 2012, JCAP, 2012, 048
Matsubara, T. 1994a, ApJL, 434, L43
Matsubara, T. 1994b, arXiv:astro-ph/9501076
Matsubara, T. 1996, ApJ, 457, 13
Matsubara, T. 2000, arXiv:astro-ph/0006269
Matsubara, T. 2003, ApJ, 584, 1
Matsubara, T., & Suto, Y. 1996, ApJ, 460, 51
McMullen, P. 1997, Rend. Circ. Palermo, 50, 259
Mecke, K. R., Buchert, T., & Wagner, H. 1994, A&A, 288, 697
Melott, A. L., Cohen, A. P., Hamilton, A. J. S., Gott, J. R. I., & Weinberg, D. H. 1989, ApJ, 345, 618
Melott, A. L., Weinberg, D. H., & Gott, J. R. I. 1988, ApJ, 328, 50
Munshi, D., Namikawa, T., McEwen, J. D., Kitching, T. D., & Bouchet, F. R. 2021, MNRAS, 507, 1421
Narayanan, V. K., & Weinberg, D. H. 1998, ApJ, 508, 440
Nusser, A., Dekel, A., Bertschinger, E., & Blumenthal, G. R. 1991, ApJ, 379, 6
Okumura, T., Hand, N., Seljak, U., Vlah, Z., & Desjacques, V. 2015, PhRvD, 92, 103516
Okumura, T., & Jing, Y. P. 2010, ApJ, 726, 5
Olszowka, V., Hund, M., Kuntermann, V., et al. 2006, SMat, 2, 1089
Park, C., Gott III, J. R., & Choi, Y. J. 2001, ApJ, 553, 33
Park, C., & Gott, J. R. 1991, ApJ, 378, 457
Park, C., Gott, J. R., Melott, A. L., & Karachentsev, I. D. 1992, ApJ, 387, 1
Park, C., & Kim, Y.-R. 2010, ApJL, 715, L185
Park, C., Pranav, P., Chingangbam, P., et al. 2013, JKAS, 46, 125
Park, C., Vogeley, M. S., Geller, M. J., & Huchra, J. P. 1994, ApJ, 431, 569
Park, H., Kim, J., & Park, C. 2010, ApJ, 714, 207
Paul, P., Clarkson, C., & Maartens, R. 2022, arXiv:2208.04819
Peacock, J. A., & Dodds, S. J. 1994, MNRAS, 267, 1020
Peebles, P. J. E. 1976, Ap&SS, 45, 3
Pranav, P., Adler, R. J., Buchert, T., et al. 2019a, A&A, 627, A163
Pranav, P., Edelsbrunner, H., van de Weygaert, R., et al. 2017, MNRAS, 465, 4281
Pranav, P., van de Weygaert, R., Vegter, G., et al. 2019b, MNRAS, 485, 4167
Raccanelli, A., Bertacca, D., Maartens, R., Clarkson, C., & Dore, O. 2016, GReGr, 48, 84
Rahman, F., Chingangbam, P., & Ghosh, T. 2021, JCAP, 07, 026
Rehse, S., Mecke, K., & Magerle, R. 2008, PhRvE, 77, 051805
Reid, B. A., Seo, H.-J., Leauthaud, A., Tinker, J. L., & White, M. 2014, MNRAS, 444, 476
Reimberg, P., Bernardeau, F., & Pitrou, C. 2016, JCAP, 2016, 048
Ryden, B. S., Melott, A. L., Craig, D. A., et al. 1989, ApJ, 340, 647
Sahni, V., Sathyaprakash, B. S., & Shandarin, S. F. 1998, ApJL, 495, L5
Santalo, L. A. 1976, Integral Geometry and Geometric Probability (Boston, TX: Addison-Wesley), 404
Schaller, F., Wagner, J., & Kapfer, S. 2020, JOSS, 5, 2538
Schmalzing, J., & Buchert, T. 1997, ApJL, 482, L1
Schmalzing, J., & Gorski, K. M. 1998, MNRAS, 297, 355
Schroder-Turk, G. E., Kapfer, S., Breidenbach, B., Beisbart, C., & Mecke, K. 2010, JMic, 238, 57
Schroder-Turk, G. E., Mickel, W., Kapfer, S. C., et al. 2013, NJPh, 15, 083028
Scoccimarro, R. 2004, PhRvD, 70, 083007
Secrest, N. J., Hausegger, S. v., Rameez, M., et al. 2021, ApJL, 908, L51
Secrest, N. J., von Hausegger, S., Rameez, M., Mohayaee, R., & Sarkar, S. 2022, ApJL, 937, L31
Shaw, J. R., & Lewis, A. 2008, PhRvD, 78, 103512
Shivshankar, N., Pranav, P., Natarajan, V., et al. 2015, ITVCG, 22, 17451
Szalay, A. S., Matsubara, T., & Landy, S. D. 1998, ApJL, 498, L1
Szapudi, I. 2004, ApJ, 614, 51
Tomita, H. 1986, PThPh, 76, 952
Tonegawa, M., Park, C., Zheng, Y., et al. 2020, ApJ, 897, 17
van de Weygaert, R., et al. 2011a, arXiv:1110.5528
van de Weygaert, R., Vegter, G., Edelsbrunner, H., et al. 2011b, Trans. Comput. Sci., 14, 60
Villaescusa-Navarro, F., Hahn, C., Massara, E., et al. 2020, ApJS, 250, 2
Watts, P., & Coles, P. 2003, MNRAS, 338, 806
Weinberg, D. H., Gott, J. R. I., & Melott, A. L. 1987, ApJ, 321, 2
Weinberg, D. H., Mortonson, M. J., Eisenstein, D. J., et al. 2013, PhR, 530, 87
White, M., Reid, B., Chuang, C.-H., et al. 2014, MNRAS, 447, 234
Wilding, G., Nevenzeel, K., van de Weygaert, R., et al. 2021, MNRAS, 507, 2968
Yoo, J., & Seljak, U. 2014, MNRAS, 447, 1789
Zaroubi, S., & Hoffman, Y. 1996, ApJ, 462, 25
Zunckel, C., Gott, J. R., III, & Lunnan, R. 2011, MNRAS, 412, 1401